The American Journal of Pathology, Vol. 193, No. 10, October 2023

ELSEVIER

The American Journal of
PATHOLOGY

ajp.amjpathol.org

MUSCULOSKELETAL PATHOLOGY

Aberrations in Energetic Metabolism and Stress-Related Pathways Contribute to Pathophysiology in the *Neb* Conditional Knockout Mouse Model of Nemaline Myopathy

Rebecca A. Slick,[*,†,‡] Jennifer A. Tinklenberg,[*,†,‡] Jessica Sutton,[*] Liwen Zhang,[§] Hui Meng,[*] Margaret J. Beatka,[*] Mark Vanden Avond,[*,†] Mariah J. Prom,[*] Emily Ott,[*] Federica Montanaro,[¶,||] James Heisner,[†,**] Rafael Toro,[††] Henk Granzier,[‡‡] Aron M. Geurts,[†,§§] David F. Stowe,[†,**,¶¶] R. Blake Hill,[††] and Michael W. Lawlor[*,†]

From the Division of Pediatric Pathology,[*] Department of Pathology and Laboratory Medicine and Neuroscience Research Center, the Departments of Physiology,[†] Anesthesiology,[**] Biochemistry,[††] and Biomedical Engineering,[¶¶] the Clinical and Translational Science Institute,[‡] and the Mellowes Center for Genomic Sciences and Precision Medicine,[§§] Medical College of Wisconsin, Milwaukee, Wisconsin; the Mass Spectrometry and Proteomics Facility,[§] Campus Chemical Instrument Center, The Ohio State University, Columbus, Ohio; the Dubowitz Neuromuscular Centre,[¶] Molecular Neurosciences Section, Developmental Neuroscience Research and Teaching Department, UCL Great Ormond Street Institute of Child Health, London, United Kingdom; the NIHR Great Ormond Street Hospital Biomedical Research Centre,[||] London, United Kingdom; and the College of Medicine,[‡‡] University of Arizona, Tucson, Arizona

Accepted for publication
June 8, 2023.

Address correspondence to
Michael W. Lawlor, M.D.,
Ph.D., Medical College of
Wisconsin, 8701 W. Watertown
Plank Rd., Milwaukee, WI
53226.
E-mail: mlawlor@mcw.edu.

Nemaline myopathy (NM) is a genetically and clinically heterogeneous disease that is diagnosed on the basis of the presence of nemaline rods on skeletal muscle biopsy. Although NM has typically been classified by causative genes, disease severity or prognosis cannot be predicted. The common pathologic end point of nemaline rods (despite diverse genetic causes) and an unexplained range of muscle weakness suggest that shared secondary processes contribute to the pathogenesis of NM. We speculated that these processes could be identified through a proteome-wide interrogation using a mouse model of severe NM in combination with pathway validation and structural/functional analyses. A proteomic analysis was performed using skeletal muscle tissue from the *Neb* conditional knockout mouse model compared with its wild-type counterpart to identify pathophysiologically relevant biological processes that might impact disease severity or provide new treatment targets. A differential expression analysis and Ingenuity Pathway Core Analysis predicted perturbations in several cellular processes, including mitochondrial dysfunction and changes in energetic metabolism and stress-related pathways. Subsequent structural and functional studies demonstrated abnormal mitochondrial distribution, decreased mitochondrial respiratory function, an increase in mitochondrial transmembrane potential, and extremely low ATP content in *Neb* conditional knockout muscles relative to wild type. Overall, the findings of these studies support a role for severe mitochondrial dysfunction as a novel contributor to muscle weakness in NM. *(Am J Pathol 2023, 193: 1528–1547; https://doi.org/10.1016/j.ajpath.2023.06.009)*

Supported in part by A Foundation Building Strength and in part by the National Institute for Health and Care Research Great Ormond Street Hospital Biomedical Research Centre (F.M.). The Fusion Orbitrap instrument used for proteomics analysis was supported by NIH grant S10 OD018056.

R.A.S. and J.A.T. contributed equally to this work.

Disclosures: M.W.L. is the founder, CEO, and owner of Diverge Translational Science Laboratory. M.W.L. is or has recently been a member of advisory boards for Solid Biosciences, Taysha Gene Therapies, Astellas Gene Therapies (formerly Audentes Therapeutics), and Ichorion Therapeutics. M.W.L. is also a consultant for Astellas Gene Therapies (formerly Audentes Therapeutics), Encoded Therapeutics, Modis Therapeutics, Lacerta Therapeutics, Dynacure, AGADA Biosciences, Affinia Therapeutics, Biomarin, Locanabio, and Vertex Pharmaceuticals. M.W.L. receives research support from Astellas Gene Therapies, Solid Biosciences, Kate Therapeutics,

https://doi.org/10.1016/j.ajpath.2023.06.009

Nemaline myopathy (NM) is a congenital myopathy that affects 1 in 50,000 children[1] and is related to mutations in at least 14 genes.[2,3] Pathogenic variants of the *NEB* gene, which encodes nebulin, account for approximately 50% of NM cases (*NEB*-NM).[4–8] Nebulin regulates the length of the sarcomeric thin filament by acting as a molecular ruler to establish a minimal length for filamentous actin.[9–12] At the light microscopic or ultrastructural level, NM is diagnosed on the basis of the presence of nemaline rods in skeletal muscle,[13] which are composed of z-disk proteins, including α-actinin, actin, and nebulin.[2] Muscle biopsy in patients with *NEB*-NM typically shows sarcomeric disorganization and changes in thin filament length.[11]

NM is clinically heterogeneous; it has clinical variability in patients, either within the same family or with the same causative mutation.[14–16] NM can be classified by clinical presentation, but there is a general lack of correlation between genetic causes and clinical presentations in that NM presents with a broad range of disease severities.[15] Studies of animal and human NM tissue have identified various primary causes of weakness, including abnormalities of thin filament length,[10,11,17] cross-bridge cycling,[18] calcium sensitivity,[19–21] and actin-tropomyosin interactions.[22] Although these mechanisms contribute to muscle weakness, they do not fully explain the variability in symptomatic severity seen across patients with NM. As specific mutations and modes of inheritance have offered few correlations to clinical presentation and disease course,[14] identifying relevant secondary factors could lead to improved prognostic capabilities and the identification of novel treatment targets.

Because approximately half of NM cases are due to mutations in *NEB*,[23] the nebulin conditional knockout (*Neb* cKO) mouse model offers a useful opportunity to identify secondary factors that contribute to unexplained variability in NM. The *Neb* cKO mouse is born with normal levels of nebulin, which slowly decrease until approximately 5% expression remains by 5 weeks of life.[12] These animals exhibit severe myopathy with key phenotypic features, including nemaline body formation, severe weakness, and early mortality, with only half of the animals surviving to 9 weeks of age.[12,24]

We hypothesized that the common pathologic end point of nemaline rods (despite diverse genetic causes), along with the unexplained range of muscle weakness, suggests that shared secondary processes contribute to the pathogenesis of NM. Herein, these processes were investigated through a proteome-wide interrogation using the *Neb* cKO mouse model of severe NM in combination with pathway validation and structural/functional analyses (Figure 1).

As NM is a disease of protein aggregation, the current study used a proteomics approach to identify secondary processes contributing to disease severity. Skeletal muscle was isolated from *Neb* cKO mice and their wild-type (WT) counterparts at 9 weeks of age for mass spectrometric analysis. A differential expression analysis and Ingenuity Pathway Core Analysis revealed processes predicted to be perturbed in the *Neb* cKO mouse; these included mitochondrial dysfunction associated with changes in energetic metabolism and stress-related pathways. Subsequent structural and functional studies supported these data, showing structural abnormalities related to mitochondrial morphology and distribution on pathologic studies and functional abnormalities related to mitochondrial respiration and ATP content on a subset of functional assays. Overall, these findings are supportive of mitochondrial dysfunction as a contributor to the pathophysiology of weakness in nemaline myopathy.

Materials and Methods

Live Animal Studies

All studies using animal tissue were approved by the Institutional Animal Care and Use Committee at the Medical College of Wisconsin (Milwaukee, WI). Genotyping was performed as previously described.[24] Nine-week–old male and female mice that were homozygous for the floxed Cre-positive nemaline allele (*Neb* cKO) and mice that were homozygous for the Cre-positive WT allele (control animals, WT) were used for all described studies. Animals were sacrificed by CO_2 and cervical dislocation. Quadriceps and triceps were dissected, weighed, and frozen in liquid nitrogen–cooled isopentane, as previously described.[25]

Protein Sample Preparation for Proteomic Analysis

Frozen quadriceps muscle tissue was ground in liquid nitrogen. A total of 1 mL of 10% trichloroacetic acid per 100 mg tissue was added in acetone containing 2% mercaptoethanol and mixed by inverting the tube 10 times. Proteins were then precipitated overnight at −20°C. Precipitated protein was centrifuged at 5000 × *g* for 30 minutes at 4°C, washed three times in ice-cold acetone, and air dried. Pellets were frozen at −80°C until use.

Prothelia, Cure Rare Disease, and Ultragenyx. R.B.H. and R.T. have financial interest in Cytegen, a company developing therapies to improve mitochondrial function. However, the research described herein was not supported by Cytegen nor was/is in collaboration with the company. All other authors have no conflicts of interest to disclose.

The views expressed are those of the author(s) and not necessarily those of the National Health Service, the National Institute for Health and Care Research, or the Department of Health.

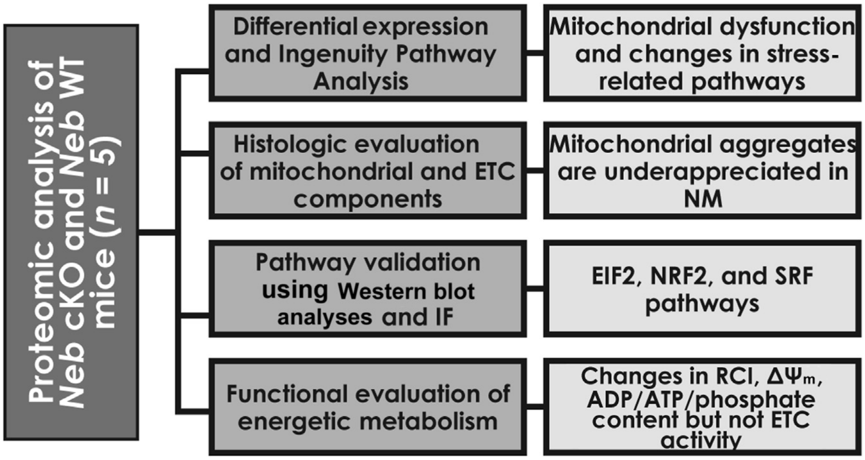

Figure 1 Schematic of experimental design. Quadriceps muscles from *Neb* conditional knockout (cKO) and wild-type (WT) mice were isolated for proteomic and differential expression analyses. Ingenuity Pathway Analysis was used to determine perturbed pathways and determined changes in metabolic and stress-related pathways. These studies were followed up by pathway validation and structural and functional assays to determine their relevance to *Neb* nemaline myopathy (NM) pathophysiology. $n = 5$ *Neb* cKO and WT mice. $\Delta\Psi_m$, mitochondrial transmembrane potential; EIF2, eukaryotic translation initiation factor 2; ETC, electron transport chain; IF, immunofluorescence; NRF2, nuclear factor erythroid 2–related factor 2; RCI, respiratory control index; SRF, serum response factor.

Protein Digestion and Peptide Fractionation

The protein pellets were weighed out and digested with trypsin (protein/enzyme, 100:1) with a final concentration of 0.1% *Rapi*Gest (Waters Corp., Milford, MA) in 50 mmol/L ammonium bicarbonate. Briefly, 5 μL of 5 μg/μL dithiothreitol in 50 mmol/L ammonium bicarbonate solution was added to the samples, and the sample was incubated at 65°C for 15 minutes, followed by the addition of 5 μL of 15 μg/μL iodoacetamide in 50 mmol/L ammonium bicarbonate solution (incubated at room temperature for 15 minutes in the dark). Sequencing-grade trypsin was added, and digestion was performed overnight at 37°C. The following day, trifluoroacetic acid was added to a final concentration of 0.5%, and the samples were incubated at 37°C for 30 minutes to precipitate *Rapi*Gest. Samples were clarified at 15,000 × *g* for 5 minutes in a microcentrifuge, supernatant was dried in a vacufuge, and supernatant was resuspended in 20 μL of 50 mmol/L acetic acid. Peptides were desalted using C18 ZipTip (Millipore Sigma, Burlington, MA), and the concentration of the peptides was determined by Nanodrop (absorbance 280 nm; Thermo Fisher Scientific, Waltham, MA).

Liquid Chromatography—MS/MS Analysis

Before tandem mass spectrometry (MS/MS), samples were subjected to online two-dimensional liquid chromatography separation using a Thermo Fisher Scientific Ultimate 3000 2D RSLC nano system. Samples (12 μg) were first fractionated on a 5 mm × 300-μm BEH C18 column with 5-μm particle size and 130-Å pore size. Solvent A was composed of 20 mmol/L ammonium formate (pH 10), and solvent B was composed of 100% acetonitrile. Peptides were eluted from column in eight successive fractions using 9.5%, 12.4%, 14.3%, 16.0%, 17.8%, 19.7%, 22.6%, and 50% of solvent B. Each eluted fraction was then trapped, diluted, neutralized, and desalted on a μ-Precolumn Cartridge (Thermo Fisher Scientific) for the second-dimension online separations performed with a 15 cm × 75-μm PepMap C18 column (Thermo Fisher Scientific) with 3-μm particle size and 100-Å pore size. For peptide separation, the flow rate was 500 μL/minute. The gradient was as follows: 0 to 5 minutes, 2% solvent B; 5 to 38 minutes, 2% to 35% solvent B; 38 to 46 minutes, 35% to 55% solvent B; and 46 to 47 minutes, 55% to 90% solvent B. Mobile phase B was kept at 90% for 1 minute before returning back to 2%. The system was equilibrated for 11 minutes for the next separation.

MS/MS data were acquired with a spray voltage of 1.7 kV, and a capillary temperature of 275°C was used. The scan sequence of the mass spectrometer was based on the preview mode data-dependent TopSpeed method: the analysis was programmed for a full scan recorded between *m/z* 400 and 1600 and an MS/MS scan to generate product ion spectra to determine amino acid sequence in consecutive scans starting from the most abundant peaks in the spectrum for the next 3 seconds. To achieve high-mass accuracy MS determination, the full scan was performed at Fourier transform (FT) mode and the resolution was set at 120,000. The automatic gain control (AGC) target ion number for FT full scan was set at 2×10^5 ions, maximum ion injection time was set at 50 milliseconds, and microscan number was set at 1. MS/MS was performed using ion trap mode to ensure the highest signal intensity of MS2 spectra using both collision induced dissociation (CID; for 2+ and 3+ charges) and electron-transfer dissociation (for 4+ to 6+ charges) methods. The AGC Target ion number for ion trap MS2 scan was set at 1000 ions, maximum ion injection time was set at 100 milliseconds, and microscan number was set at 1. The CID fragmentation energy was set to 35%. Dynamic exclusion was enabled with an exclusion duration of 15 seconds with a repeat count of two within 30 seconds and a low mass width and high mass width of 10 parts per million (Supplemental Figure S1).

Data Analysis

Sequence information from the MS/MS data was processed by converting the .raw files into a merged file (.mgf) using an in-house program, RAW2MZXML_n_MGF_batch (merge.pl, a Perl script). The resulting .mgf files were searched using Mascot Daemon version 2.6.2 (Matrix Science, Boston, MA), and the database searched against was the most recent SwissProt mouse database. Mass accuracy of the precursor ions was set to 10 parts per million, and accidental pick of one ^{13}C peak was also included into the search. Fragment mass tolerance was set to 0.5 Da. Considered variable modifications were oxidation (Met) and deamidation (N and Q). Fixed modification is carbamidomethylation. Four missed cleavages for the enzyme were permitted. A decoy database was also searched to determine the false discovery rate, and peptides were filtered according to the false discovery rate. The significance threshold was set at $P < 0.05$, and bold red peptides were required for valid peptide identification. Only proteins identified with a minimum of two peptides as well as <1% false discovery rate were accepted for quantitation. Label-free quantitation was performed using the spectral count approach, in which the relative protein quantitation is measured by comparing the number of MS/MS spectra identified from the same protein in each of the multiple liquid chromatography (LC)–MS/MS data sets.[26] The mass spectrometry proteomics data have been deposited to the ProteomeXchange Consortium via the PRIDE[27] partner repository, with the data set identifier PXD042201. Scaffold 5.0.1 (Proteome Software Inc., Portland, OR) was used for data analysis. The *t*-test was performed by Scaffold to evaluate if the fold change for certain proteins is significant ($P < 0.05$). A fold change of <0.5 or >2 was used to define differentially expressed proteins.

PC Analysis

Principal component (PC) analysis, a dimensionality reduction technique, was used to visualize factors that contribute to variance. Data sets were loaded into R statistical computing software version 3.5.2 (*http://www.r-project.org*). Packages, including tidyr, dplyr, and magrittr, were used for data management. PC analysis was completed using the prcomp function (statistical package), which uses singular value decomposition of the data matrices. The raw data were visually assessed by scree plots using base plot functions. Data visualization of PC1 and PC2 of each data set was done using ggplot2 and RColorBrewer. Heat map scale bars were calculated using normalized rotation scores of proteins identified to contribute to PC1. The R code used for data analysis is provided in Supplemental Code 1.

Ingenuity Pathway Analysis

To evaluate protein-set enrichment, the *Neb* cKO versus WT proteomic data set was uploaded into the Ingenuity Pathway Analysis (IPA) software package version 84978992 (Qiagen, Germantown, MD). An expression (core) analysis was run using the measurement of expression fold change to calculate directionality z-scores. The confidence level was set to explore experimentally observed and highly predicted values using a $P = 0.05$ and fold change cutoffs of -1.5 and 1.5. IPA core analysis uses the Ingenuity Knowledge Base, which is an archive of biological and chemical findings that is curated, both manually and automatically, and integrated with third-party databases.[28] This is used to predict canonical pathways, mechanistic effects, and downstream effects.

Western Blot Analysis

Frozen quadriceps samples were divided into sections (8 μm thick) and homogenized in radioimmunoprecipitation assay lysis buffer (EMD Millipore, Temecula, CA) containing protease inhibitor (Roche, Basel, Switzerland) and phosphatase inhibitor (Roche). Western blot analyses were performed, as previously described,[29] to validate changes in protein levels seen in the proteomics data set. Polyvinylidene difluoride membranes were probed using antibodies against nuclear factor erythroid 2–related factor 2 (NRF2; ab137550; Abcam, Waltham, MA; 1:750), kelch-like ECH-associated protein 1 (KEAP1; ab227828; Abcam; 1:1000), NAD(P)H dehydrogenase [quinone] 1 (NQO1; ab34173; Abcam; 1:1000), serum response factor (SRF; ab53147; Abcam; 1:500), myocardin-related transcription factor A (MRTF-A; 21166-1-AP; Proteintech, Rosemont, IL; 1:500), vinculin (13901S; Cell Signaling Technology, Danvers, MA; 1:5000), eukaryotic translation initiation factor 2 (EIF2S1; ab26197; Abcam; 1:500), and phosphorylated EIF2S1 (ab131505; Abcam; 1:250). Ponceau staining was used as the standardization condition, whereas the remaining targets were used to confirm signals seen in the proteomics data set. Visualization of antibodies was completed using enhanced chemiluminescence (RPN2236; Cytivia, Emeryville, CA). Protein levels were quantified using Image Lab Software version 6.1 (Bio-Rad Laboratories, Hercules, CA), and values were normalized to total protein visualized by Ponceau staining. Total protein was used due to difficulty in finding a reliable loading control across the *Neb* cKO mouse model and its wild-type counterparts.

Histologic Evaluation

Triceps muscle from male ($n = 5$) and female ($n = 5$) mice of each genotype were used to perform all histologic analyses. Muscles were cross-sectioned (8 μm thick) and mounted onto slides. Each slide was stained with hematoxylin and eosin, Gömöri trichrome, or cytochrome oxidase (COX) using standard techniques. Images were taken using a Leica DMB6 B microscope using a Leica DFC 7000T camera and Leica LAS X standard software version 3.5.2 (Leica Microsystems, Buffalo Grove, IL), and cells were counted using ImageJ cell counter[30] version 1.53e (NIH, Bethesda, MD; *http://imagej.nih.gov/ij*, last accessed February 10, 2023) on matching ×200 images.

For electron microscopy (EM), a 2-mm thick by 10-mm long piece of quadriceps muscle was placed in an EM fixative containing 2% glutaraldehyde with 4% paraformaldehyde in sodium cacodylate buffer. After 24 hours, samples were placed in 0.1 mol/L sodium cacodylate for storage until processing and embedding for EM could be completed. Samples were submitted to the Electron Microscopy Core Facility at the Medical College of Wisconsin. Sections of epoxy resin embedded tissue were cut at 60-nm thickness and imaged on a Hitachi H600 transmission electron microscope (Hitachi, Tokyo, Japan) equipped with an AMT digital imaging system (AMT Imaging, Woburn, MA). The revealed mitochondrial ultrastructure was recorded for each sample.

Muscle IF

Muscle immunofluorescence (IF) was used to determine if evaluated pathways have abnormal protein localization in *Neb* cKO animals compared with their WT counterparts. Frozen quadriceps samples were sectioned transversely (8 μm thick), and three tissue sections were mounted per slide. Tissue sections were stained with primary antibodies NRF2 (ab137550; Abcam; 1:200), KEAP1 (ab227828; Abcam; 1:150), NQO1 (ab34173; Abcam; 1:200), MRTF-A (21166-1-AP; Proteintech; 1:200), EIF2 (ab26197; Abcam; 1:500), alpha-actinin 3 (ACTN3; 9B5; Creative Biolabs, Shirley, NY; 1:250), and DAPI (H3570; Invitrogen, Waltham, MA; 1:30,000). Secondary antibodies include goat anti-rabbit IgG Alexa Fluor 594 (A11012; Invitrogen; 1:400) and goat anti-mouse IgG1 Alexa Fluor 488 (A21121; Invitrogen; 1:400). Images were taken using a Leica SP8 Upright Confocal Microscope using Leica LAS X standard software version 3.5.2.

Fiber typing was performed using mouse monoclonal antibodies against type 2a fast myosin (SC-71; Developmental Studies Hybridoma Bank, Iowa City, IA; 1:100), type 1 slow myosin (BA-D5; Developmental Studies Hybridoma Bank; 1:500), and laminin (L9393; Sigma Aldrich, St. Louis, MO; 1:300). Secondary antibodies used were Alexa Fluor 647 goat anti-rat IgG (A-21247; Thermo Fisher; 1:400), rhodamine red x-conjugated AffiniPure goat anti-mouse IgG2a (115-295-206; Jackson ImmunoResearch Inc., West Grove, PA; 1:400), Alexa Fluor 488 goat anti-mouse IgG1 (A-21121; Thermo Fisher; 1:400), Alexa Fluor 594 goat anti-mouse IgG2b (A-21145; Thermo Fisher; 1:400), and Alexa Fluor 647 donkey anti-rabbit (A-31573; Thermo Fisher; 1:400). Images were taken using a Leica DMB6 B microscope with a Leica DFC 7000T camera using Leica LAS X standard software version 3.5.2.

Isolation of Mitochondria from Muscle Tissue

A modified standard protocol was used for mitochondrial isolation from skeletal muscle.[31] Mice were euthanized using CO_2, and the quadriceps, hamstrings, gastrocnemius, triceps, and masseter muscles were quickly removed and pooled from three animals for each experimental replicate because tissue masses of <600 mg resulted in insufficient material to assess mitochondrial function. Because of this need to pool muscles from multiple animals and small litters of *Neb* cKO mice, sex differences could not be examined. The tissue was rinsed with ice-cold isolation buffer containing 200 mmol/L mannitol, 50 mmol/L sucrose, 5 mmol/L KH_2PO_4, 5 mmol/L 3-(N-morpho1ino)propanesulfonate (MOPS), 1 mmol/L EGTA, and 0.1% bovine serum albumin (pH adjusted to 7.15 with KOH). Tissue was then minced in approximately 5 mL isolation buffer and homogenized until smooth using a THb Handheld Tissue Homogenizer (Omni International, Inc., Lake Villa, IL). Samples were then centrifuged at 700 × *g* for 10 minutes at 4°C. The supernatant was removed and spun at 10,500 × *g* for 10 minutes at 4°C. The new supernatant was poured off, and the resulting pellet was resuspended in 500 μL isolation buffer. The final suspension was spun again at 10,500 × *g* for 10 minutes at 4°C to ensure the purity of the sample. The final supernatant was discarded, and the pellet was resuspended in isolation buffer to a volume of approximately 100 μL. A Bradford Assay (Bio-Rad Laboratories; number 5000202) was performed on the isolated mitochondria sample to determine protein concentration.

Respiratory Control Index

Oxygen consumption was measured using a Clark Oxygen Electrode (model S 200A; Strathkelvin Instruments, Glasgow, Scotland). The isolated mitochondrial sample (22 μL at 12.5 mg/mL) was added to the experimental buffer containing 130 mmol/L KCl, 5 mmol/L K_2HPO_4, 20 mmol/L MOPS, and 0.1% bovine serum albumin (528 μL buffer, for a total volume of 550 μL) and allowed to equilibrate for 1 minute. After the oxygen reading was stable, 5.5 μL glutamate/malate solution was added for a final buffer concentration of 20 mmol/L. After an additional minute, 5.5 μL ADP solution was added for a final buffer concentration of 250 mmol/L. Oxygen content in the electrode chamber decreases rapidly as mitochondrial respiration accelerated during oxidative phosphorylation.

ETC Enzyme Functional Assays

Mitochondrial isolations, as described above, were used for all electron transport chain (ETC) enzyme activity assays. Assays for complexes I through V were performed per the manufacturers' instructions (Abcam ab109721, ab109908, ab109905, and ab109911; Cayman Chemical, Ann Arbor, MI, number 701000) with minor modifications in some cases. Each sample was run in duplicate, and details of the assays are summarized in Table 1. Assays were optimized using WT mouse mitochondrial isolates and bovine heart mitochondria before beginning the analyses on test tissue. Bovine heart mitochondrion was run as a positive control for every test to ensure the assay was working properly. Each enzyme activity assay measures the colorimetric change in absorbance over time, in which the slope of the line is proportional to enzyme activity. With the exception of complex III, all sample protein concentrations were adjusted to 5.5 mg/mL before beginning the experiment. Samples that had concentrations of <5.5 mg/mL were excluded from further experimentation.

ATP, ADP, and Phosphate Assays

The ATP (Abcam; ab83359), ADP (Abcam; ab83355), and phosphate (Abcam; ab65622) assays were performed per the manufacturer's instructions on fresh mouse tissue with a few minor changes, including the addition of a lower concentration standard curve for some assays. The amount of tissue extract used was adjusted per sample to ensure the sample reading was on either the high or the low standard curve. Experimental parameters are outlined in Table 2. Concentrations of ATP, ADP, or phosphate were calculated on the basis of the standard curve, calculated per μL of sample, and then normalized to the average total protein of the original samples.

Mitochondrial Transmembrane Potential

Mitochondrial transmembrane potential ($\Delta\Psi_m$) was determined using an Isolated Mitochondria Staining Kit (Sigma, Sauk Village, IL; CS0760), per the manufacturer's instructions. Mitochondria were isolated as described above, and protein was determined via Bradford assay. Isolates were diluted so that 5 μg of protein was loaded per well. Red fluorescence was measured at excitation (490 nm)/emission (590 nm) for the JC-1 (5,5,6,6′-tetrachloro-1,1′,3,3′ tetraethylbenzimi-dazoylcarbocyanine iodide) aggregates, and green fluorescence excitation (485 nm)/emission (535 nm) was measured for JC-1 monomers.[32] The ratio of red/green fluorescence was used to determine relative $\Delta\Psi_m$, with a higher ratio equivalent to a higher (more negative) $\Delta\Psi_m$.

Statistical Analysis

Prism 9.1.2 software (GraphPad, Inc., La Jolla, CA) was used to perform all statistical tests aside from proteomic analysis. An unpaired *t*-test was performed between genotypes. Significance for all experiments was set to $P < 0.05$, and data are presented as the means ± SEM.

Results

Mass Spectrometry

For this study, it was particularly important to extract proteins from all cellular compartments with the same efficiency from wild-type and NM muscles to identify differences in protein abundance. Muscles typically contain large amounts of insoluble matrix and structural contractile proteins that can be inconsistently extracted between samples, making it difficult to accurately assess and compare expression levels. Furthermore, NM muscles contain nemaline rods made of protein aggregates that are difficult to extract. To minimize the effect of differences in protein solubility between *Neb* WT and cKO samples, protein extraction was optimized first. A trichloroacetic acid/acetone extraction buffer used to isolate hard to solubilize proteins from plants[33] reproducibly and effectively extracted muscle proteins, including those contained within nemaline rods. A drawback of this high-efficiency protein extraction is that muscle structural proteins, such as myosin, actin, and titin, are present with high abundance in these samples and suppress the detection of other proteins, especially the ones with low abundance. These high abundance proteins make up a large portion of the muscle protein content. Thus, without any prefractionation, these proteins will suppress the detection of other proteins, especially the ones with low abundance in muscle samples. Hence, online two-dimensional LC was used to fractionate the peptides in muscle samples for further LC-MS/MS analysis. By analyzing each fraction separately, the complexity of samples analyzed on the LC separation column was greatly reduced and thus increased detection of low abundance proteins.[34]

Using two-dimensional LC-MS/MS, 1584 proteins were identified across all the samples (Supplemental Table S1). Besides myofibrillar proteins, such as myosin and actin, other proteins, such as the ones present in nemaline rods, including α-actinin, actin, tropomyosin, myotilin, γ-filamin, cofilin-2, telethonin, and nebulin, were all identified with good sequence coverage. Among them, 1213 proteins were proteins common in both *Neb* cKO and WT groups, and 367 were unique proteins identified only in the *Neb* cKO group. More than 250 of them were detected in at least four of five biological replicates with good sequence coverage. The three unique proteins detected in the WT groups were not reproducible (only one protein, ankyrin-1, was detected in four of five replicates) and had poor sequence coverage. This observation suggests that *Neb* cKO muscles express the same subset of proteins as wild-type muscles, but additionally have high protein content of a subset of proteins that are either absent or expressed at a level below the detection limit in WT muscles. This observation suggested, in general, a global increase in protein content in *Neb* cKO quadriceps tissues, although phenotypically they have a reduction in myofiber size. This indicates that proteins may be mislocalized to protein aggregates and functioning aberrantly.

Differential Expression Analysis and Data Visualization

Of the proteins identified, 844 had an increase in expression and 17 had a decrease in expression (Figure 2A). Because of the number of proteins in the data set, there were many proteins that had an infinite fold change or a $P < 0.00010$,

Table 1 Protocol Specifications for Each Mitochondrial Assay

Protocol element	Complex I	Complex II	Complex III	Complex IV	Complex V
Manufacturer (product number)	Abcam (ab109721)	Abcam (ab109908)	Abcam (ab109905)	Abcam (ab109911)	Cayman Chemical (number 701000)
Plate type	Immunocapture	Immunocapture	96 Well	Immunocapture	1/2 Volume 96 Well
Detergent extraction	Yes	Yes	No	Yes	No
Initial protein concentration, mg/mL	5.5	5.5	1.2	5.5	5.5
Final protein concentration	300 μg/mL	1 mg/mL	0.09 mg/mL	25 μg/mL	25 μg/200 μL
Incubation	3 Hours	2 Hours + 30 minutes with lipids (dark)	N/A	3 Hours	N/A
Reaction solution	NADH, dye	Ubiquinone, succinate, DCPIP	Succinate, cytochrome *c*, KCN, rotenone	Cytochrome *c*	Enzyme mix, ATP, NADH, rotenone
Wavelength, nm	450	600	550	550	340
Test length, minutes	30	60	20	120	3
Analysis time	20 Minutes	10 Minutes	5 Minute	7 Minutes	12 Seconds
Shaking	Yes	No	No	No	No
Temperature	Room temperature	Room temperature	Room temperature	30°C	25°C

Kits were used per the manufacturer's protocol.
DCPIP, 2,6-dichlorophenolindophenol; KCN, potassium chloride; N/A, not applicable.

which appear as vertical lines on the border of the volcano plot. The skewed number of proteins with an increase in content in the proteomic profile was expected because of the presence of protein aggregates in NM muscle tissue. To confirm this, an IPA pathway was built using proteins known to localize to nemaline rods and grown based solely on protein-protein interactions of proteins differentially expressed in the *Neb* cKO data set. Most proteins in the network were significantly increased (Supplemental Figure S2). This suggests that many yet to be identified proteins accumulate in protein aggregates based on protein-protein interactions in NM, resulting in a global increase in protein levels in the *Neb* cKO data set. Protein content related to predicted pathways may probably be affected while the pathway is still functioning properly. Nonetheless, identifying these proteins may lead to advancements in prognostic capabilities and a better understanding of disease progression. Therefore, although the proteomics comparisons are biased by the presence of protein aggregates, the data were cautiously used as a guide to identify relevant processes for further study.

PC analysis was performed to identify PCs that contribute to variability within the data set (Figure 2B). PC1 contributed to 53.8% variability and separated the *Neb* cKO from WT samples. Proteins that make up PC1 were involved in Gene Ontology and biological processes, including cell-cell adhesion, glycolysis, ATPase activity, intrinsic apoptotic signaling pathway in response to oxidative stress, regulation

Table 2 Summary of ATP, ADP, and Phosphate Assay Protocols

Protocol element	ATP	ADP	Phosphate
Manufacturer (product number)	Abcam (ab83355)	Abcam (ab83359)	Abcam (ab65622)
Plate type	96 Well	96 Well	96 Well
Standard curve	High and low	High and low	High
Sample buffer	ATP assay buffer	ADP assay buffer	Tris-buffered saline
Sample buffer volume	1000 μL (WT), 500 μL (cKO)	1000 μL (WT), 500 μL (cKO)	1000 μL (WT), 1000 μL (cKO)
Muscle	2 Triceps	2 Triceps	2 Triceps
Homogenize	Yes	Yes	Yes
Centrifuge (4°C)	5 Minutes at 13,000 × *g*	5 Minutes at 18,000 × *g*	15 Minutes at 18,000 × *g*
Sample volume (total), μL	50	50	200
Background mix	Probe, developer	Probe, developer	N/A
Reaction mix	Probe, converter, developer	Probe, converter, developer	Phosphate reagent
Reaction mix volume, μL	50	50	30
Incubation time (dark), minutes	30	30	30
Wavelength, nm	570	570	650

Kits were used per the manufacturer's protocol.
cKO, conditional knockout; N/A, not applicable; WT, wild type.

of reactive oxygen species, metabolic processes, and neuromuscular junction development (Supplemental Table S2).[35] Enrichr analysis revealed that the top 20 proteins in PC1 were related to pathways such as the unfolded protein response ($P = 0.0027$), cycling of GTP-binding nuclear protein Ran in nucleocytoplasmic transport ($P = 0.00499$), ethanol oxidation ($P = 0.010$), fatty acid ω-oxidation ($P = 0.015$), β-alanine metabolism ($P = 0.022$), transcription termination factor Rho (Rho) cell motility signaling pathway ($P = 0.022761$), ascorbate and aldarate metabolism ($P = 0.026$), histidine metabolism ($P = 0.029$), fatty acid metabolism ($P = 0.041$), and glycerolipid metabolism ($P = 0.048$) (Supplemental Tables S2 and S3). PC2 accounted for 17.3% of the variability in the data set but separated all WT and four *Neb* cKO samples from the fifth *Neb* cKO sample (Figure 2B). Of the top 20 proteins, 19 were not differentially expressed because of the variably high count from the separated *Neb* cKO sample (Supplemental Table S3).

Of the 844 detected proteins with an increase in content in the *Neb* cKO data set, 219 had an infinite fold change and significant *P* value because of being present below the level of detection in the comparator WT data set. These 219 proteins are related to processes involved in regulation of nuclear division and myotube fusion. The top 28 of these proteins, based on rotation score, are depicted as a heat map in Figure 2C. On the basis of Enrichr, these 28 proteins are related to pathways such as β-oxidation of long-chain fatty acids, α-linolenic and linoleic metabolism, and peroxisomal lipid metabolism, pointing to changes in the overall metabolic profile of *Neb* cKO mice compared with their WT counterparts.

Pathways Predicted to Be Affected by IPA

The five top canonical pathways predicted to be affected included EIF2 signaling, mitochondrial dysfunction, oxidative phosphorylation, sirtuin signaling pathway, and regulation of EIF4 and P70S6K signaling (Table 3). As with Enrichr analysis, most pathways expected to be altered by IPA were processes related to translation initiation and regulation in response to stress and energetic metabolism. Protein ubiquitination and calcium signaling were also pathways of interest. However, because of the number of metabolic pathways that were predicted to be affected, these pathways were interrogated further to determine potential links to secondary processes that contribute to NM pathophysiology.

Protein content related to the IPA canonical pathways of glycolysis, gluconeogenesis, and tricarboxylic acid cycle, as well as protein levels of each ETC complex, was further assessed. Content of proteins that play a role in glycolysis and gluconeogenesis was decreased, whereas proteins in the tricarboxylic acid cycle and all complexes of the ETC had

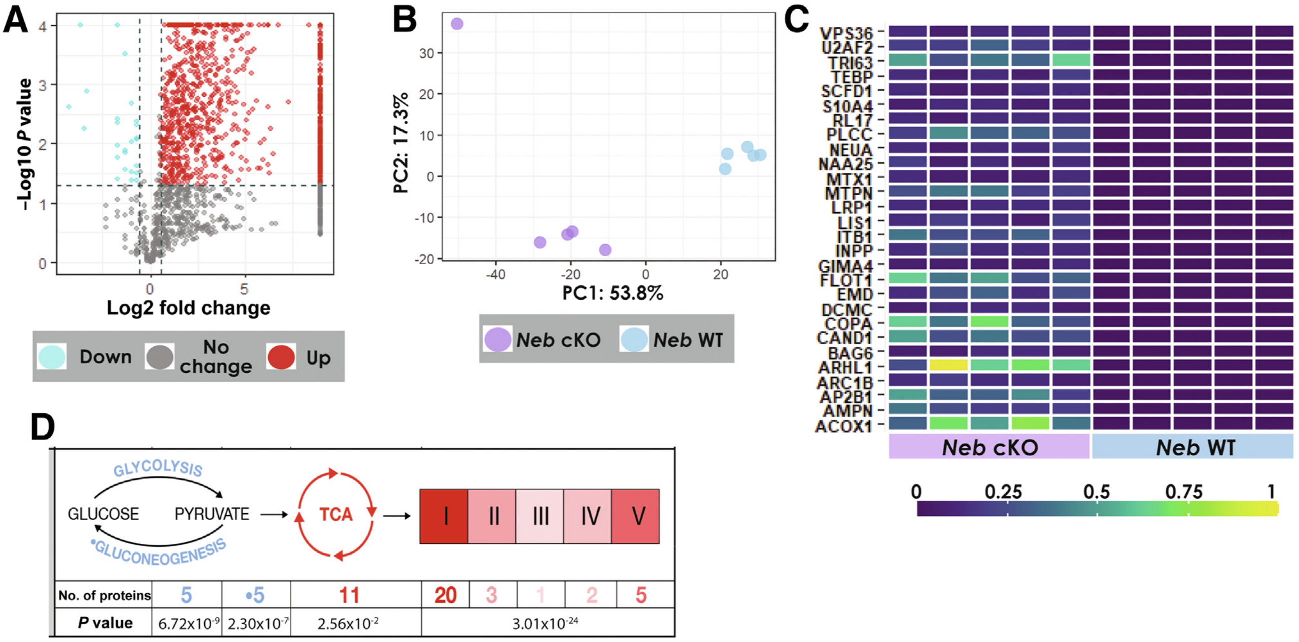

Figure 2 Pathway analysis indicates metabolism and stress-related processes are perturbed in *Neb* nemaline myopathy. **A:** Volcano plot representing differentially expressed proteins in the *Neb* conditional knockout (cKO) quadriceps versus their wild-type (WT) counterpart. **Dashed lines** represent boundaries for differentially expressed proteins, defined by the parameters of a fold change of <0.5 or >1.5 with a $P \leq 0.05$. **B:** Principal component (PC) analysis of *Neb* cKO versus WT differential expression data sets, where PC1 accounts for 53.8% of variability within the data set. **C:** Heat map representing the top 28 proteins detected solely in *Neb* cKO samples that contribute to data set variability. **D:** Protein expression in pathways related to energetic metabolism are altered in the *Neb* cKO mice. Increases in protein expression are depicted in shades of red, and decreases in protein expression are depicted in shades of blue. TCA, tricarboxylic acid.

an increase in protein content (Figure 2D). NM resulted in changes in protein content related to metabolism in a model of severe *Neb* cKO NM, which may contribute to disease phenotypes.

Pathway Validation

Following proteomic and bioinformatic analyses, top relevant pathways identified by IPA were probed using Western blot and IF. Together, these techniques provide complementary approaches, as the pathway analysis assesses pathway activity, the Western blot assesses protein content, and the IF stains assess protein localization. An upstream regulator, one important inhibitor or coregulator, and a downstream transcription factor were chosen to be analyzed in the NRF2, SRF, and EIF2 pathways. Proteins not shown did not have interpretable results via Western blot analyses and/or IF.

Nuclear Factor Erythroid 2—Related Factor 2

The changes in metabolism seen in the *Neb* cKO mouse model may result in increased oxidative stress within the muscle cells and produce the resulting changes in the NRF2 pathway. Upstream analysis in IPA predicted that NRF2 was activated in the *Neb* cKO model (z-score = 7.743; $P = 1.37 \times 10^{-27}$). Pathways that would be affected by NRF2 activation were then investigated in IPA to look for downstream effects of NRF2 activation and were shown to be affected to different degrees (Supplemental Figure S3). In addition, all proteins of the NRF2 network present in the differential expression data set were differentially expressed (Supplemental Table S4).

Protein levels of NRF2 itself were increased in *Neb* cKO compared with those in WT mice ($P = 0.0039$) (Figure 3, A and D). Proteomics data indicate that NRF2 was activated, which under normal conditions would not result in increased KEAP1 protein content.[36,37] However, KEAP1 protein content was increased in *Neb* cKO mice ($P = 0.0018$) (Figure 3, B and E). NQO1, a downstream transcriptional target of NRF2 activation, was also investigated by Western blot. NQO1 had an increase in protein levels in *Neb* cKO mice ($P = 0.0030$) (Figure 3, C and F). Protein localization was assessed by IF with costains of the protein of interest, ACTN3 (to indicate nemaline rods), and DAPI (to indicate nuclei). KEAP1 and NQO1 were normally localized to the cytosol, whereas NRF2 was localized to the cytosol when inactive and the nucleus when active in WT mice, as shown in Figure 3G. NRF2, KEAP1, and NQO1 all had changes in cellular localization and formed their own aggregates, as well as colocalized with nemaline rods in some areas, as indicated by ACTN3 (Figure 3G). KEAP1 localization was the most affected, showing extremely increased intensity and localization to aggregates and nemaline rods. The change in protein content of KEAP1 and its localization to aggregates indicated its aberrant function in NRF2 (Figure 3G). Altogether, these results confirmed that critical NRF2 pathway proteins were abnormal in protein content and/or localization, suggesting that the NRF2-mediated stress response pathway was anomalous in *Neb*-NM.

Table 3 Top Five Canonical Pathways Predicted to Be Affected by IPA in the *Neb* cKO Mice

Top canonical pathways: *Neb* cKO versus WT		
Name	*P* value	Overlap
EIF2 signaling	3.76×10^{-35}	61/232
Mitochondrial dysfunction	3.01×10^{-24}	43/171
Oxidative phosphorylation	1.13×10^{-21}	33/109
Sirtuin signaling pathway	2.70×10^{-19}	49/292
Regulation of EIF4 and p70S6K signaling	4.82×10^{-18}	36/168

A core analysis was run in IPA to determine the top canonical pathways likely to be affected in *Neb* cKO mice based off changes in protein content identified by liquid chromatography—tandem mass spectrometry.

cKO, conditional knockout; EIF, eukaryotic translation initiation factor; IPA, Ingenuity Pathway Analysis; WT, wild type.

Serum Response Factor

Because of the predicted changes in actin-related processes by IPA, it was speculated that NM mutations could secondarily affect pathways that respond to structural changes of the thin filament. Literature search identified one such pathway, the SRF pathway, which is known to regulate >200 genes related to skeletal muscle growth, function, cytoskeletal structure, metabolism, and regeneration (Figure 4A). Because mislocalization of z-disk proteins in NM could promote SRF signaling through activation of striated muscle activator of rho signaling (STARS; Figure 4A), protein content and/or localization of SRF, MRTF-A, and vinculin were evaluated by Western blot and/or IF.

SRF protein content was significantly greater in *Neb* cKO mice than their WT counterparts ($P = 0.0026$) (Figure 4, B and E). Vinculin, a downstream target of SRF, was also significantly increased in *Neb* cKO muscle tissue ($P = 0.00008$) (Figure 4, D and G). MRTF-A, the co-activator of SRF, was not significantly different between *Neb* cKO and WT mice (Figure 4, C and F). However, similar to the NRF2 pathway, MRTF-A localization was greatly altered in *Neb* cKO quadriceps tissue (Figure 4H). MRTF-A was punctate and evenly dispersed across *Neb* WT tissue, whereas it was localized to aggregates in some *Neb* cKO fibers and void in others (Figure 4H). Although overall MRTF-A content was not significantly different, MRTF-A localized to potentially novel aggregates as well as nemaline rods in *Neb* cKO tissue (Figure 4H). Overall, changes in SRF pathway protein content and localization corroborated the proteomic data and point to a role for SRF signaling in disease-related processes.

Eukaryotic Translation Initiation Factor 2

The EIF2 signaling pathway was the top canonical pathway predicted to be affected (Supplemental Figure S4, A and D)

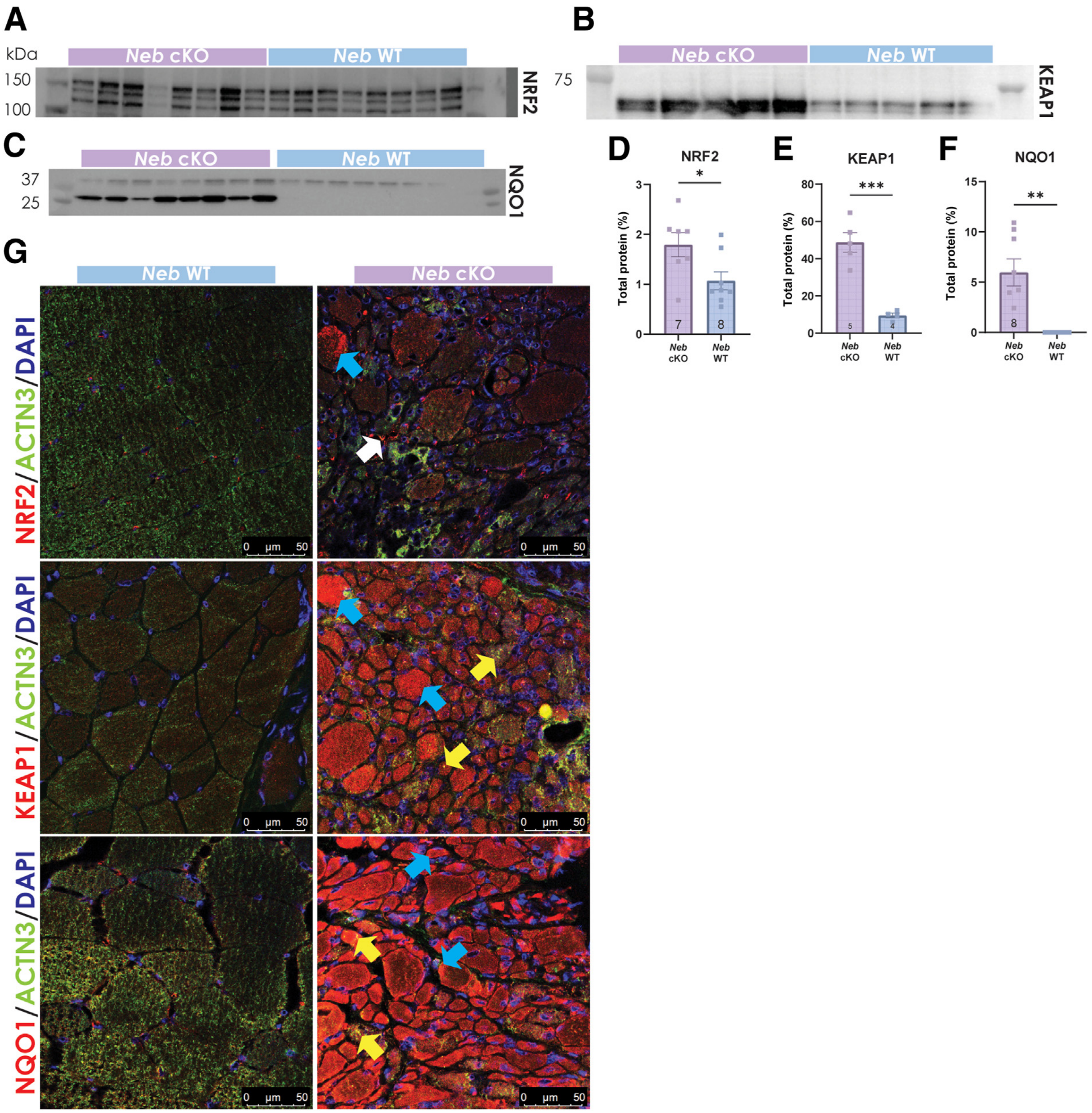

Figure 3 Protein expression and localization related to the nuclear factor erythroid 2–related factor 2 (NRF2) pathway are altered in *Neb* nemaline myopathy. **A–F:** NRF2 expression is statistically different than in wild-type (WT) mice. Kelch-like ECH-associated protein 1 (KEAP1) ($P = 0.0018$) and NAD(P)H dehydrogenase [quinone] 1 (NQO1) ($P = 0.0030$) expression levels are significantly increased in the *Neb* conditional knockout (cKO) animals versus their WT counterparts via Western blot analyses. All blots were quantified using total protein. **G:** Immunofluorescence shows NRF2, KEAP1, and NQO1 localization are altered in the *Neb* cKO mice. All three proteins appear to form their own aggregates as well as colocalize to nemaline rods shown using alpha-actinin 3 (ACTN3). (**Blue arrows** indicate individual aggregates; **yellow arrows**, colocalization with nemaline rods; and **white arrow**, nuclear localization.) $^{*}P < 0.05$, $^{**}P < 0.01$, and $^{***}P < 0.001$. Scale bars = 50 μm (**G**).

and activated by IPA (z-score = 4.747; $P = 3.76 \times 10^{-36}$). As indicated by Western blot analysis, *Neb* cKO mice had similar total EIF2 levels compared with their WT counterparts when quantified on the basis of total protein expression (Supplemental Figure S4, B and D, and Supplemental Figure S5). However, they had increased levels of phosphorylated EIF2 (Supplemental Figure S4, C and E). The increase in phosphorylated EIF2 compared with total EIF2 was statistically significant in the *Neb* cKO mice ($P = 0.0006$) (Supplemental Figure S4F). It is interesting to note that the *Neb* WT samples displayed a double band on the EIF2 Western blot, of which the lower band is speculated to be an IgG light band. Tissue sections from *Neb* cKO mice and their WT counterparts ($n = 8$) were costained using EIF2, ACTN3, and DAPI to identify potential changes in localization and colocalization with nemaline rods or nuclei. Seemingly greater EIF2 perinuclear localization was observed in *Neb* cKO mice than in WT mice but

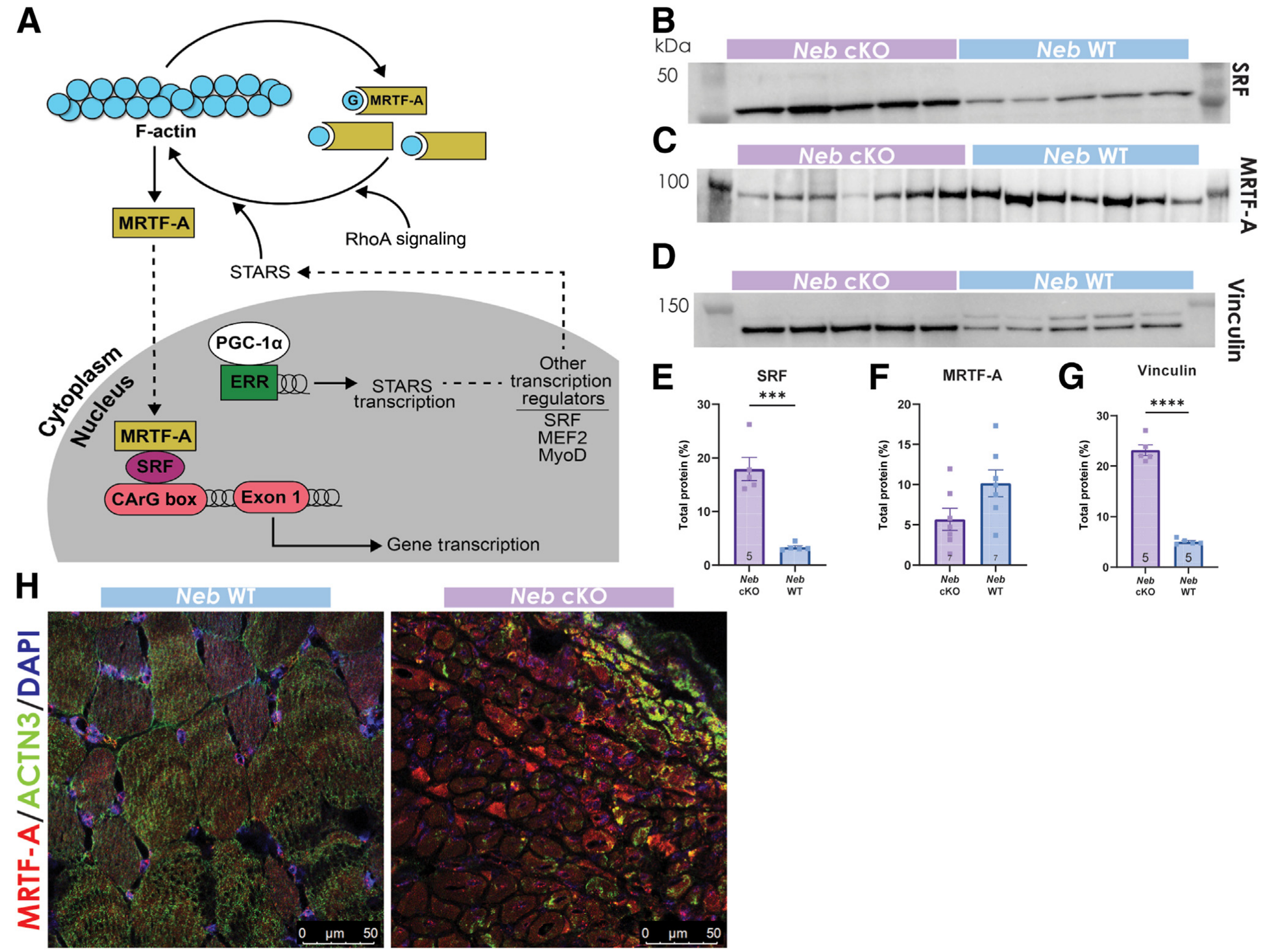

Figure 4 Proteins related to the serum response factor (SRF) pathway are altered in expression or localization in the *Neb* conditional knockout (cKO) mice. **A:** In skeletal muscle, RhoA signaling in combination with increased expression of striated muscle activator of rho signaling (STARS) are known to activate SRF target gene transcription by enhancing actin polymerization. STARS is enriched in skeletal muscle and prominently localized to the z-disk. STARS has been postulated to be a skeletal muscle mechanosensor that activates downstream SRF signaling. In addition, eukaryotic translation initiation factor 2 (EIF2) is known to activate cyclic AMP-dependent transcription factor ATF-4 (ATF4), which promotes mitochondrial biogenesis via peroxisome proliferator-activated receptor gamma coactivator 1-alpha (PGC-1α). PGC-1α binding to the steroid hormone receptor ERR (ERR) promoter can also activate STARS transcription and, therefore, SRF signaling. **B** and **E:** SRF protein expression is significantly increased in the *Neb* cKO animals. **C** and **F:** Myocardin-related transcription factor A (MRTF-A) expression is not statistically different between *Neb* cKO and wild-type (WT) mice. **D** and **G:** Vinculin expression is significantly increased in the *Neb* cKO animals. **H:** MRTF-A is mislocalized in *Neb* cKO mice, forming its own aggregates in some areas and colocalizing to nemaline rods based on alpha-actinin 3 (ACTN3) expression in other areas. $^{***}P < 0.001$, $^{****}P < 0.0001$. Scale bars = 50 μm (**H**). MEF2, myocyte-specific enhancer 2; MyoD, myoblast determination protein 1.

little to no colocalization with nemaline rods was seen (Supplemental Figure S4G). Altogether, these data validated the proteomic analysis that predicted EIF2 was activated in *Neb* cKO mice.

Histology Indicates Nemaline Rods, Mitochondrial Aggregates, and Fiber-Type Disproportion in *Neb* cKO Mice

Given that the IPA suggested issues with the tricarboxylic acid cycle and ETC, a structural evaluation of mitochondria in *Neb* cKO mice was performed, starting with a histologic evaluation using 8-μm thick sections of isopentane-frozen triceps muscle.[25] Staining using hematoxylin and eosin revealed numerous, small fibers with slightly basophilic cytoplasm and an increase in the number of internally nucleated fibers, as previously described[24] (Figure 5). Gömöri trichrome staining revealed red/purple rod-like structures within the small fiber population and compact aggregates, consistent with nemaline rods in a subpopulation of myofibers that also included the larger fiber population[24] (Figure 5). As Gömöri trichrome stains both nemaline rods and mitochondrial aggregates, staining for COX (corresponding to complex IV of the mitochondrial electron transport chain) was performed to specifically evaluate mitochondrial distribution. COX staining revealed a high signal in the small fiber population, indicating that much of the red/purple material seen on Gömöri trichrome in these cells corresponded to mitochondria. Within the larger fiber population, the COX stain revealed an unusual pattern of focal mitochondrial aggregation in some fibers, with periphery aggregation in the subsarcolemmal region (Figure 5). Together, the Gömöri trichrome and COX stains indicate that a significant number of the inclusions that may include nemaline rods are also locations of mitochondrial aggregation (Figure 5 and Table 4). These findings were further confirmed using EM. The EM images showed an increase in mitochondrial aggregation, extreme structural disorganization, and a close association of the nemaline rods with mitochondrial aggregation (Supplemental Figure S6A). Lastly, fiber typing showed an increase in oxidative fibers in the *Neb* cKO animals (Supplemental Figure S6B) that has been previously reported.[12]

Mitochondrial Assays

Mitochondrial Respirometry

Predicted changes in mitochondrial function by proteomics and structural analyses of *Neb* cKO tissue led to the interrogation of mitochondrial function. Mitochondrial

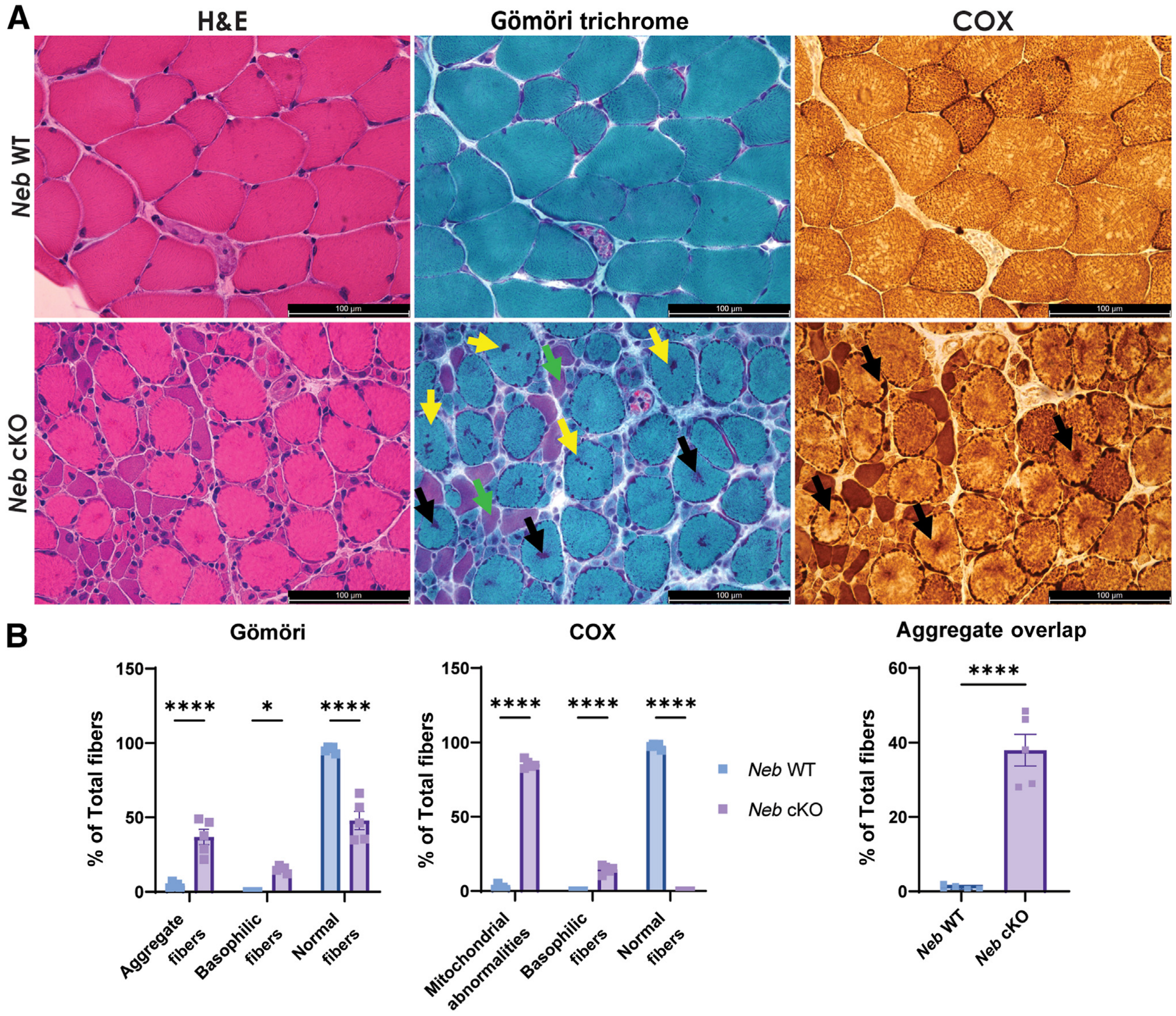

Figure 5 Histologic changes in the *Neb* conditional knockout (cKO) mouse. **A:** *Neb* cKO mice have a decrease in fiber size and show significant nemaline pathology on Gömöri trichrome staining compared with wild-type (WT) animals. *Neb* cKO animals also show mitochondrial aggregation and changes in mitochondrial distribution on the cytochrome oxidase (COX) stain. **B:** *Neb* cKO animals show significant increases in the percentage of fibers with aggregates and percentage of basophilic fibers and a decrease in the percentage of normal fibers on Gömöri trichrome stain. The same pattern is seen on the COX stain. The *Neb* cKO animal shows a significant overlap in the number of aggregates seen in the Gömöri trichrome and COX stains. Examples of nemaline rods (**yellow arrows**), mitochondrial aggregates (**black arrows**), and basophilic fibers (**green arrows**) are highlighted. $^{*}P < 0.05$, $^{****}P < 0.0001$. Scale bars = 100 µm (**A**). H&E, hematoxylin and eosin.

respirometry is a method commonly used to assess the overall function of isolated mitochondria. Oxygen content is measured over time. The slope of the line during state 3 (active, ADP-stimulated respiration) over the slope of the line in state 4 (after ADP is exhausted) was used to determine the respiratory control index (RCI) (Supplemental Figure S7A). RCI is an arbitrary number; however, it is used as an overall measure of mitochondrial function, with higher RCI values correlating to healthier mitochondria and lower values indicating mitochondrial dysfunction.[38] The RCI values of the *Neb* cKO animals showed a significant decrease in mitochondrial respiration when compared with their WT counterparts (*Neb* WT versus *Neb* cKO: 8.0 ± 0.6 versus 2.9 ± 0.3; $P < 0.0001$) (Figure 6A, Supplemental Figure S7B, and Table 5, which indicates a severe mitochondrial deficiency.

Evaluation of Electron Transport Chain and Its By-products

To pinpoint the cause of mitochondrial functional deficiencies, each complex of the ETC was examined for overall enzyme activity. Complex enzyme activities were measured by assessing the change in OD per time (minute) in the most linear portions of their graphs (Supplemental Figure S7C). Interestingly, no significant differences were seen between WT and *Neb* cKO ETC enzyme activities in any of the complexes (Figure 6F and Table 6). However, significant decreases were seen in the amount of phosphate (*Neb* WT versus *Neb* cKO: 7.81 ± 1.60 versus 3.95 ± 1.53 normalized [Phos] nmol/μL; $P = 0.006$) and ADP (*Neb* WT versus *Neb* cKO: 1.62 ± 0.11 versus 1.13 ± 0.08 normalized [ADP] nmol/μL; $P = 0.005$) (Figure 6, B and C, and Table 5) in tissue homogenates. ATP content was undetectable in *Neb* cKO homogenates (*Neb* WT versus *Neb* cKO: 1.01 ± 0.12 versus 0.00 ± 0.00 normalized [ATP] nmol/μL; $P < 0.0001$) (Figure 6D and Table 5) and, subsequently, the ATP to ADP concentration, [ATP]/[ADP] ratio, was significantly decreased in the *Neb* cKO animals (*Neb* WT versus *Neb* cKO: 0.62 ± 0.06 versus 0.00 ± 0.00 [ATP]/[ADP]; $P < 0.0001$). These data complemented the finding of low RCIs in *Neb* cKO animals, indicating poor capacity for ATP generation.

Mitochondrial transmembrane potential was performed using JC-1 dye, which emits a green fluorescence as a monomer but accumulates in the mitochondria where it forms J aggregates that emit red fluorescence.[32] An increased red/green ratio in the *Neb* cKO mouse (red/green relative fluorescence unit = 2.01 ± 0.18), compared with *Neb* WT animals (red/green relative fluorescence unit = 1.15 ± 0.13; $P = 0.0085$), indicated a greater positive $\Delta\Psi_m$ in knockout animals (Figure 6E and Table 5). This increase in $\Delta\Psi_m$ was associated with a markedly reduced capacity for oxidative phosphorylation and is also compatible with low [ATP]/[ADP] ratios.

Discussion

Primary and Secondary Disease Processes in NM

Genetically, 14 genes associated with NM have been identified thus far, with several clinical cases still genetically unresolved.[2,3,7] Although typically classified by causative mutation, this classification does not predict the severity or prognosis of the disease.[15,16,39] Several studies have shown clinical variability of patients in either the same family or with the same causative mutation.[14–16] One particular study showed that multiple patients with the same mutation were classified into different clinical severity categories.[16] Another case study including a father and son with the same confirmed mutation had vastly different clinical courses.[14] Altogether, specific mutations and modes of inheritance have offered few correlations to clinical presentation and disease course.[14] The ubiquity of nemaline rods suggests that unidentified secondary processes impact disease severity and are shared across patients with NM regardless of primary genetic cause and muscle weakness.

Studies of animal and human *Neb*-NM tissue have identified various primary causes of weakness that contribute to disease phenotypes. The protein nebulin is thought of as a molecule that modulates thin filament length as it spans the entire length of the thin filament.[40] Primary structural defects of nebulin mutations include altered thin filament

Table 4 Mitochondrial Aggregates May Be Underrecognized in NM

	Neb WT		*Neb* cKO		*Neb* WT versus *Neb* cKO
Variable	% Total fibers	SEM	% Total fibers	SEM	*P* value
Fibers with aggregates	4.17	0.89	36.82	5.18	<0.0001
Nonuniform mitochondrial distribution	2.51	0.75	85.49	1.23	<0.0001
Basophilic fibers (Gömöri trichrome stain)	0.00	0.00	21.00	5.64	0.0362
Basophilic fibers (COX stain)	0.00	0.00	14.51	1.23	<0.0001
Overlap	0.90	0.33	37.95	4.25	<0.0001

The percentage of fibers with aggregates and basophilic fibers significantly increases in the *Neb* cKO mouse, whereas the percentage of normal fibers on Gömöri trichrome and COX staining decreases. *Neb* cKO animals also show a significant overlap in the number of aggregates seen via Gömöri trichrome and COX stains.

cKO, conditional knockout; COX, cytochrome oxidase; NM, nemaline myopathy; WT, wild type.

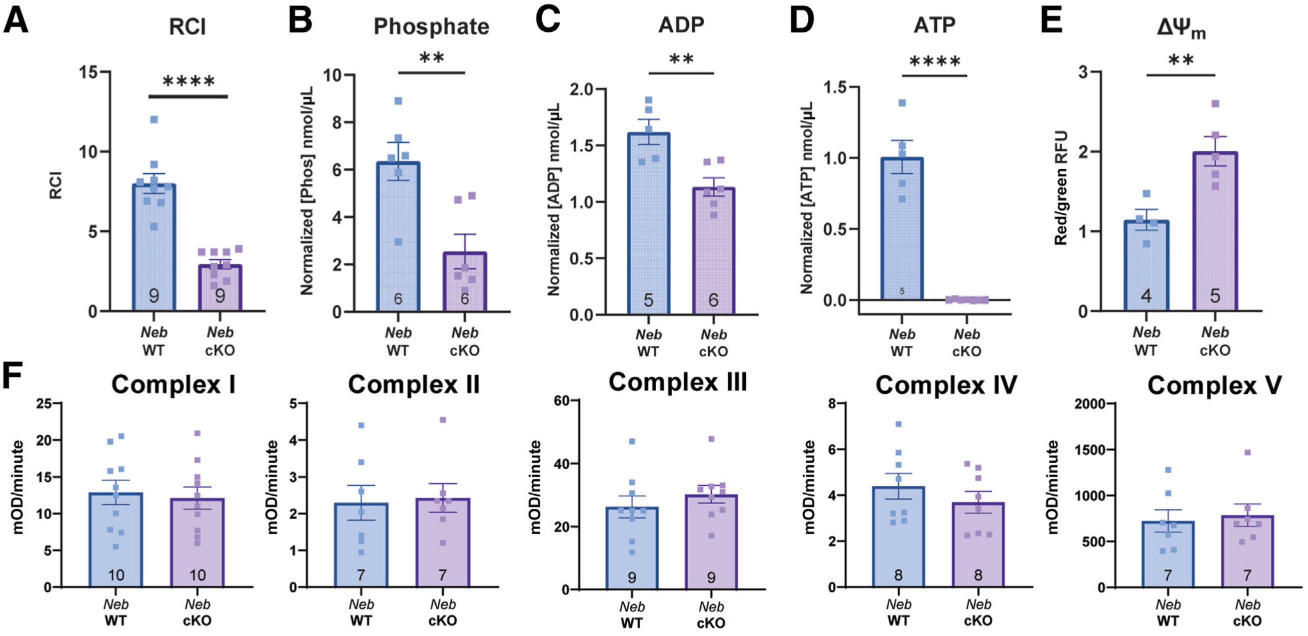

Figure 6 Mitochondrial phenotype in the *Neb* conditional knockout (cKO) mouse. **A:** *Neb* cKO animals have a significant decrease in respiratory control index (RCI) values compared with *Neb* wild-type (WT) animals. **B–E:** The *Neb* cKO animals have significant changes in the amount of phosphate (**B**), ADP (**C**), and ATP (**D**) as well as an increase of the red/green ratio of JC-1 (5,5,6,6′-tetrachloro-1,1′,3,3′ tetraethylbenzimi-dazoylcarbocyanine iodide), indicating a significant increase in transmembrane potential (**E**) compared with WT animals. **F:** The *Neb* cKO mouse shows no changes in any electron transport chain enzyme activity compared with WT animals. $^{**}P < 0.01$, $^{****}P < 0.0001$. $\Delta\Psi_m$, mitochondrial transmembrane potential; mOD, milli-optical density.

length[10,11,17] and myofibrillar disorganization, and may affect interactions with proteins, including f-actin–capping protein (CAPZ),[41] desmin, myopalladin,[42,43] tropomodulin,[44] α-actinin, and titin.[43] In addition, changes in nebulin structure or expression alter actin-tropomyosin interactions.[22] These structural abnormalities contribute to changes in cross-bridge cycling[18] and calcium sensitivity.[19–21] Altogether, these primary structural and functional changes result in inefficient contraction and muscle weakness. However, these primary defects do not fully explain the variability seen in *Neb*-NM, which led to the speculation that secondary processes contribute to NM pathogenesis, which was tested using the *Neb* cKO mouse.

Secondary disease processes are sequelae of the primary genetic defect that contribute to disease phenotypes. Primary disease processes in NM, related to the causative gene, may contribute to muscle weakness by sarcomeric disorganization and inefficient cross-bridge cycling, thus causing downstream effects that could explain the heterogeneity seen across animal models and patients. To elucidate these secondary processes, a novel approach was applied using combinatorial proteomic, bioinformatic, structural, and functional assessments. The current study shows that this approach is capable of identifying aberrant secondary processes in a mouse model of severe NM that can be further tested via structural and functional assays as indicators of disease.

Experimental Approach and Implications in NM

Proteomics was identified as being a suitable high-throughput technique for this study, as NM is a disease of protein aggregation, and this technique would be sensitive to issues of abnormal protein expression or accumulation. Previous studies using proteomics in muscle tissue have proven it to be a reliable high-throughput approach for determining alterations in protein content in physiological and pathologic states and for generating new

Table 5 *Neb* cKO Mice Display Significant Changes in Overall Mitochondrial Health and Levels of Metabolic By-Products

Variable	RCI	SEM	Phosphate	SEM	ADP	SEM	ATP	SEM	$\Delta\Psi_m$	SEM
Neb WT	8.35	0.69	7.81	1.60	1.62	0.11	1.00	0.12	1.15	0.13
Neb cKO	5.45	0.32	3.95	1.53	1.13	0.08	0.00	0.00	2.01	0.18
P value	<0.0001		0.0056		0.0053		<0.0001		0.0085	

RCI and phosphate/ATP/ADP contents are significantly decreased in *Neb* cKO mitochondrial isolates compared with their WT counterparts, whereas $\Delta\Psi_m$ is increased.

$\Delta\Psi_m$, mitochondrial transmembrane potential; cKO, conditional knockout; RCI, respiratory control index; WT, wild type.

Table 6 No Significant Changes Were Seen in ETC Activity in *Neb* cKO Mitochondrial Isolates

	Complex I		Complex II		Complex III		Complex IV		Complex V	
Variable	mOD/minute	SEM	mOD/minute	SEM	mOD/minute	SEM	mOD/minute	SEM	mOD/minute	SEM
Neb WT	12.90	1.65	2.29	0.48	26.25	3.45	4.39	0.57	723.70	122.90
Neb cKO	12.12	1.52	2.43	0.39	30.21	2.80	3.69	0.47	786.20	123.20
P value	0.7333		0.8294		0.3858		0.3559		0.7253	

cKO, conditional knockout; ETC, electron transport chain; mOD, milli-optical density; WT, wild type.

hypotheses.[45,46] In this study, proteomic and bioinformatic analyses revealed that changes in protein content in the *Neb* cKO mouse were consistent with abnormal changes in metabolic pathways, as well as oxidative and global stress pathways. To substantiate these data, changes in protein content were first confirmed via Western blot analyses and alterations in protein localization were studied using immunofluorescence. These studies were followed by structural and functional assays to determine if secondary metabolic changes contribute to NM phenotypes.

Protein Content and Localization in Metabolic and Stress-Related Pathways Are Altered in *Neb*-NM

In a disease of protein aggregation, changes in protein content do not necessarily equal the degree of protein activation or function. A variety of cell stressors can lead to changes in native protein folding,[47–49] so, although protein levels may be significantly altered, it is unclear if they are in their native states and properly functioning. In the current study, the proteomics results show that proteins downstream of EIF2 are increased 1.5-fold to infinite-fold. NRF2 and

Table 7 *Neb* cKO Mice Have Abnormalities in Protein Content or Localization in Stress-Related and Metabolic Pathways That May Contribute to NM Pathophysiology

Pathway	EIF2	NRF2	SRF
Function	Converging factor in ISR activated by SR or metabolic stress, calcium dysregulation, and amino acid deprivation.[50]	Master regulator of oxidative stress response.[51] Also involved in metabolism, mitochondrial bioenergetics, mitochondrial content and function, and skeletal muscle integrity.[52–54]	Controls expression of >200 genes related to muscle development, regeneration, and contractility.[55,56] It is also linked to actin dynamics.[57]
Previously described roles in muscle pathophysiology	Previously implicated in dermatomyositis, RYR1-related myopathies, myasthenia gravis, and muscular dystrophies.[58–63]	Mitochondrial abnormalities have been reported in NM: complex I deficiencies, abnormally sized/distributed mitochondria, and mitochondrial aggregates.[64–68]	Decreased SRF contributes to muscle fiber atrophy and decreased capacity to regenerate.[55] Increased expression contributes to insulin resistance.[69] Defects in SRF signaling previously reported in *ACTA1*-NM.[70]
Abnormal elements in *Neb*-NM	EIF2 is abnormally distributed. pEIF2 expression is significantly increased, indicating activation.	Abnormal protein expression and localization of NRF2, KEAP1, and NQO1.	SRF and vinculin protein expression levels are increased, and MRTF-A is abnormally localized.
Possible roles in *Neb*-NM	Secondary process activated in response to primary contractile dysfunction and SR stress, resulting from sarcomeric disorganization and protein misfolding.	Contractile dysfunction leads to energy deficits that result in abnormal mitochondrial phenotypes, triggering the oxidative stress response.	Stress response downstream of mitochondrial bioenergetics activated as a master regulator of muscle gene programming.

The NRF2, SRF, and EIF2 pathways were shown to be affected to varying degrees in *Neb* cKO samples.

cKO, conditional knockout; EIF2, eukaryotic translation initiation factor 2; KEAP1, kelch-like ECH-associated protein 1; ISR, integrated stress response; MRFT-A, myocardin-related transcription factor A; NM, nemaline myopathy; NQO1, NAD(P)H dehydrogenase [quinone] 1; NRF2, nuclear factor erythroid 2–related factor 2; pEIF2, phosphorylated EIF2; RYR1, ryanodine receptor 1; SR, sarcoplasmic reticulum;; SRF, serum response factor.

SRF were not detected by mass spectrometry, but downstream protein content signatures point to both proteins being activated in *Neb* cKO muscle as compared to their WT counterparts. Western blot analyses of phosphorylated EIF2, NRF2, SRF, and co-activators or downstream proteins showed a global increase in protein content in these pathways (Figures 3 and 4, Supplemental Figure S4, and Table 7[50–70]). However, immunofluorescence of these proteins showed that proteins of interest either aggregated in their own aggregates or colocalized with nemaline rods (Figures 3 and 4, Supplemental Figure S4, and Table 7). Data showed that many proteins were capable of forming aggregates in *Neb*-NM tissue independent of nemaline rods which could be identified on the basis of proteomic signatures. In the current study, abnormal levels or distribution of EIF2, NRF2, or SRF pathway proteins were identified. Further investigation is necessary to determine how perturbations in these pathways play a role in NM. It is likely that many of the proteins with an increase in content are being caught in protein aggregates and not performing their classic functions.[50–70]

Parallel studies interrogated pathways across two *Acta1* mouse models of NM (the KI.*Acta1*$^{\mathrm{H40Y}}$ and Tg*ACTA1*$^{\mathrm{D286G}}$ models where KI refers to knock-in and Tg refers to transgenic) of varying severity to determine whether changes in protein content and localization in these pathways were indicative of disease severity. NRF2, SRF, and EIF2 pathway protein content and localization were altered in a severity-dependent manner, with Tg*ACTA1*$^{\mathrm{D286G}}$ samples being the least abnormal, KI.*Acta1*$^{\mathrm{H40Y}}$ samples being moderately abnormal, and *Neb* cKO samples being the most abnormal.[71] Therefore, protein aggregation in these pathways appeared to increase with disease severity and was not a result of pathogenic variants in a specific causative gene.

Mitochondrial Abnormalities Contribute to *Neb*-NM

Top canonical pathways showed differential expression in proteins related to glycolysis, gluconeogenesis, the tricarboxylic acid cycle, and ETC between *Neb* cKO and *Neb* WT animals, indicating variable abnormalities of metabolic function (Figure 2). Muscle is a highly metabolic tissue that relies heavily on mitochondrial ATP production to maintain contractile function; therefore, changes in energy production and availability may play key roles in disease pathophysiology. Changes in mitochondrial numbers and localization,[64,72–74] structural abnormalities,[75,76] and increases in energy expenditure[77,78] have been previously reported in NM mouse models. In addition, studies in post-natal hyperoxia, Huntington disease,[79,80] insulin resistance,[81] and traumatic brain injury[82] have all shown changes in mitochondrial complex activity in pathologic processes. Therefore, it is possible that similar alterations in mitochondrial biology may be isolated in NM models.

The three most common histologic stains for mitochondrial disease are the Gömöri trichome (which shows ragged red fibers), the succinate dehydrogenase stain (which shows the location of succinate dehydrogenase, complex II), and the COX stain (which shows the activity of cytochrome *c* oxidase, or complex IV).[83] COX is particularly useful because different protein subunits are encoded in either the mitochondrial DNA or nuclear DNA, and the staining pattern can reflect deficiencies in those subunits.[83] Some abnormalities in staining that are traditionally associated with adult mitochondrial dysfunction (such as the presence of COX-negative fibers) are not a feature of most biopsies harboring mitochondrial disease in children. There have been reports of mixed nemaline-mitochondrial myopathy[64,72] and nemaline rods appearing in primary mitochondrial disease[73] dating back to the 1980s, but mitochondrial function had yet to be thoroughly investigated in NM. Here, traditional mitochondrial stains and assessments were used on the *Neb* cKO mouse model of NM to identify a mitochondrial phenotype.

Structural analysis of the mitochondria related to nemaline body burden has been identified in NM[64,72,83] but has not been systematically studied. This may be in part because of the similarities in staining patterns of rods and mitochondrial structures seen in the routine pathologic assessments, such as the Gömöri trichrome stain. The current study shows that pathologic inclusions include mitochondrial aggregates in association with and separate from nemaline rods. Previous studies in the KI.*Acta1*$^{\mathrm{H40Y}}$ mouse have shown structural abnormalities, including increases in mitochondrial size and number on EM as a potential cause of the animals' decrease in force generation due to the displacement of functional sarcomeres.[75] The similarly displaced and reorganized mitochondria in the *Neb* cKO animals may be contributing to their extreme phenotype of muscle weakness,[24] but a more direct assessment of mitochondrial localization may be needed to confirm these findings.

RCI and ETC function assays were performed to investigate any alterations in the function of the mitochondria. Although the *Neb* cKO animals show a severely deficient mean RCI value when compared with WT animals, the exact cause remains unclear. A common reason for the decrease in respiratory function in primary mitochondrial disease is a decrease in function of a specific ETC complex, which is what was expected here. Surprisingly, however, when systematic function of the isolated ETC complex enzymes were examined, no significant changes were seen between the WT and *Neb* cKO animals. The enzyme assay that was used for complex V tests its ability to pump protons back across the inner mitochondrial transmembrane and not its ability to produce ATP. It is, therefore, possible that its functionality as an ATPase remains intact, but its abilities as an ATP synthase are inhibited, thus explaining the low levels of ATP in tissue isolates.

Low [ATP]/[ADP] ratios are known to drive mitochondrial respiration, drive ATP synthesis, and maintain $\Delta\Psi_m$ at a level lower than maximum (-140 to -180 mV).[84] High levels of ATP inhibit complex IV to maintain $\Delta\Psi_m$ at approximately −120 mV through a negative feedback mechanism. In low [ATP]/[ADP] conditions, complex IV is not inhibited, and if $\Delta\Psi_m$ is depolarized, ATPase results in proton pumping (H^+ efflux), which, with complexes I, III, and IV, tends to repolarize $\Delta\Psi_m$, but to a submaximal level. Normally, complex V uses the proton motive force (H^+ influx) to produce ATP, which stimulates respiration to maintain $\Delta\Psi_m$.[84−86] In a stressed system where ATP is not being generated or used, $\Delta\Psi_m$ will remain high.[85] If complex V is not generating ATP, the [ATP]/[ADP] ratio remains low, and complex IV does not reduce oxygen to water (ie, respiration is reduced). Although the ATP synthase activity of complex V was not able to be tested, the increases in cellular stress pathways (Table 3), normal function of the ETC complexes, undetectable levels of ATP, and a higher $\Delta\Psi_m$ suggest that complex V was unable to produce sufficient ATP in muscle tissue of *Neb* cKO animals.

In addition, it is possible that NM muscle requires more ATP in either the active or the passive state, which may account for the extreme lack of adenosine nucleotides. Changes in energy expenditure have been documented in *Acta1*-NM animal models using magnetic resonance imaging, phosphocreatine production, ATP consumption, and force generation.[77,78] These studies concluded that, although the ratios of phosphocreatine/ATP were not significantly different between WT and mutant groups, the mutant animals had lower force production and, therefore, a higher overall energy cost.[77,78] In addition, a recent study from Ranu et al[87] determined that *NEB*-NM muscle fibers had impairments in the myosin superrelaxed state, which contribute to increased energy consumption at rest in affected muscle fibers. This increase in ATP consumption in a resting state may help explain why ETC function appears to remain intact, whereas ATP content is severely depleted, in *Neb* cKO muscle.

Limitations

As with any study, there were limitations to the study described here. First, the *Neb* cKO model does not perfectly recapitulate the genetic defects seen in humans as patients with NM typically have a stable deficiency in nebulin levels rather than progressive nebulin depletion.[12,88,89] In addition, although both male and female animals were used in the experiments, sex differences were not evaluated because of the small size of the *Neb* cKO animals and the frequent need to pool tissue from multiple available animals at each time point. Although the *Neb* cKO mouse model does not fully recapitulate human disease, and sex differences could not be evaluated because of hypotrophic muscle, it is currently the most useful mouse model in studying severe *Neb*-NM because of its symptomatic severity and the marked deficiency of nebulin that it produces. Because this was a large study, comparisons were not reported between different time points or models. For pathway studies, the degree of protein content is not equivalent to the degree of activation. In addition, there were differences seen between mass spectrometry, Western blot analysis, and immunofluorescence results (when comparing protein content in mass spectrometry and Western blot and when comparing protein amounts to immunofluorescence signals). It is possible that discrepancies between mass spectrometry results and Western blot analyses relate to differences in protein isolation protocols between these two assays. It is possible that the protein isolation used for mass spectrometry was better able to capture nemaline rods compared with that with Western blot. However, as protein isolation was not a component of the immunofluorescence studies, it was useful to pursue immunofluorescence investigations of possible proteins of interest regardless of the Western blot data. In some cases, proteins of interest were abnormally localized to protein aggregates and so the inclusion of all three data sets provides complementary information and questions of interest for future research in this area. Future studies are necessary to mechanistically dissect the EIF2, NRF2, and SRF pathways in NM.

Conclusions and Future Directions

Nemaline myopathy is an extremely heterogeneous disease in which prognosis cannot be predicted and no current treatments exist. The unexplained heterogeneity led to the speculation that secondary processes play a role in disease pathogenesis. A comprehensive approach was used to identify perturbed processes based on changes in protein content and determined that energetic metabolism and stress-related pathways were affected in *Neb*-NM animals. Specifically, RCI and phosphate, ADP, and ATP levels were severely reduced, whereas $\Delta\Psi_m$ was significantly increased. In addition, protein levels and/or localization in the EIF2, NRF2, and SRF pathways were perturbed in *Neb* cKO tissue. In the future, the EIF2, NRF2, and SRF pathways will be studied *in vitro* to identify whether changes in these pathways play a role or are a consequence of NM pathophysiology. Future studies will also need to give a more comprehensive assessment of mitochondrial number and mitochondrial homeostatic mechanisms, such as fusion and fission.

Supplemental Data

Supplemental material for this article can be found at *http://doi.org/10.1016/j.ajpath.2023.06.009*.

References

1. North KN, Laing NG, Wallgren-Pettersson C: Nemaline myopathy: current concepts: the ENMC International Consortium and Nemaline Myopathy. J Med Genet 1997, 34:705−713
2. Sewry CA, Laitila JM, Wallgren-Pettersson C: Nemaline myopathies: a current view. J Muscle Res Cell Motil 2019, 40:111−126

3. Kondo E, Nishimura T, Kosho T, Inaba Y, Mitsuhashi S, Ishida T, Baba A, Koike K, Nishino I, Nonaka I, Furukawa T, Saito K: Recessive RYR1 mutations in a patient with severe congenital nemaline myopathy with ophthalomoplegia identified through massively parallel sequencing. Am J Med Genet A 2012, 158a: 772−778
4. Pelin K, Donner K, Holmberg M, Jungbluth H, Muntoni F, Wallgren-Pettersson C: Nebulin mutations in autosomal recessive nemaline myopathy: an update. Neuromuscul Disord 2002, 12:680−686
5. Pelin K, Hilpela P, Donner K, Sewry C, Akkari PA, Wilton SD, Wattanasirichaigoon D, Bang ML, Centner T, Hanefeld F, Odent S, Fardeau M, Urtizberea JA, Muntoni F, Dubowitz V, Beggs AH, Laing NG, Labeit S, de la Chapelle A, Wallgren-Pettersson C: Mutations in the nebulin gene associated with autosomal recessive nemaline myopathy. Proc Natl Acad Sci U S A 1999, 96:2305−2310
6. Pelin K, Wallgren-Pettersson C: Nebulin–a giant chameleon. Adv Exp Med Biol 2008, 642:28−39
7. Wallgren-Pettersson C, Sewry CA, Nowak KJ, Laing NG: Nemaline myopathies. Semin Pediatr Neurol 2011, 18:230−238
8. Malfatti E, Romero NB: Nemaline myopathies: state of the art. Rev Neurol (Paris) 2016, 172:614−619
9. Labeit S, Gibson T, Lakey A, Leonard K, Zeviani M, Knight P, Wardale J, Trinick J: Evidence that nebulin is a protein-ruler in muscle thin filaments. FEBS Lett 1991, 282:313−316
10. Gokhin DS, Bang ML, Zhang J, Chen J, Lieber RL: Reduced thin filament length in nebulin-knockout skeletal muscle alters isometric contractile properties. Am J Physiol Cell Physiol 2009, 296: C1123−C1132
11. Ottenheijm CA, Witt CC, Stienen GJ, Labeit S, Beggs AH, Granzier H: Thin filament length dysregulation contributes to muscle weakness in nemaline myopathy patients with nebulin deficiency. Hum Mol Genet 2009, 18:2359−2369
12. Li F, Buck D, De Winter J, Kolb J, Meng H, Birch C, Slater R, Escobar YN, Smith JE 3rd, Yang L, Konhilas J, Lawlor MW, Ottenheijm C, Granzier HL: Nebulin deficiency in adult muscle causes sarcomere defects and muscle-type-dependent changes in trophicity: novel insights in nemaline myopathy. Hum Mol Genet 2015, 24:5219−5233
13. North KN, Laing NG, Wallgren-Pettersson C: Nemaline myopathy: current concepts. The ENMC International Consortium and Nemaline Myopathy. J Med Gene 1997, 34:705−713
14. Bouldin AA, Parisi MA, Laing N, Patterson K, Gospe SM Jr: Variable presentation of nemaline myopathy: novel mutation of alpha actin gene. Muscle Nerve 2007, 35:254−258
15. Sanoudou D, Beggs AH: Clinical and genetic heterogeneity in nemaline myopathy–a disease of skeletal muscle thin filaments. Trends Mol Med 2001, 7:362−368
16. Wallgren-Pettersson C, Pelin K, Nowak KJ, Muntoni F, Romero NB, Goebel HH, North KN, Beggs AH, Laing NG: Genotype-phenotype correlations in nemaline myopathy caused by mutations in the genes for nebulin and skeletal muscle alpha-actin. Neuromuscul Disord 2004, 14:461−470
17. Witt CC, Burkart C, Labeit D, McNabb M, Wu Y, Granzier H, Labeit S: Nebulin regulates thin filament length, contractility, and Z-disk structure in vivo. EMBO J 2006, 25:3843−3855
18. Chandra M, Mamidi R, Ford S, Hidalgo C, Witt C, Ottenheijm C, Labeit S, Granzier H: Nebulin alters cross-bridge cycling kinetics and increases thin filament activation: a novel mechanism for increasing tension and reducing tension cost. J Biol Chem 2009, 284: 30889−30896
19. de Winter JM, Buck D, Hidalgo C, Jasper JR, Malik FI, Clarke NF, Stienen GJ, Lawlor MW, Beggs AH, Ottenheijm CA, Granzier H: Troponin activator augments muscle force in nemaline myopathy patients with nebulin mutations. J Med Genet 2013, 50:383−392
20. Lee EJ, De Winter JM, Buck D, Jasper JR, Malik FI, Labeit S, Ottenheijm CA, Granzier H: Fast skeletal muscle troponin activation increases force of mouse fast skeletal muscle and ameliorates weakness due to nebulin-deficiency. PLoS One 2013, 8:e55861
21. Ottenheijm CA, Hooijman P, DeChene ET, Stienen GJ, Beggs AH, Granzier H: Altered myofilament function depresses force generation in patients with nebulin-based nemaline myopathy (NEM2). J Struct Biol 2010, 170:334−343
22. Marttila M, Hanif M, Lemola E, Nowak KJ, Laitila J, Gronholm M, Wallgren-Pettersson C, Pelin K: Nebulin interactions with actin and tropomyosin are altered by disease-causing mutations. Skelet Muscle 2014, 4:15
23. Qiu B, Ruston J, Granzier H, Justice MJ, Dowling JJ: Failure to identify modifiers of NEBULIN-related nemaline myopathy in two pre-clinical models of the disease. Biol Open 2019, 8:bio044867
24. Tinklenberg JA, Siebers EM, Beatka MJ, Fickau BA, Ayres S, Meng H, Yang L, Simpson P, Granzier HL, Lawlor MW: Myostatin inhibition using ActRIIB-mFc does not produce weight gain or strength in the nebulin conditional KO mouse. J Neuropathol Exp Neurol 2019, 78:130−139
25. Meng H, Janssen PML, Grange RW, Yang L, Beggs AH, Swanson LC, Cossette SA, Frase A, Childers MK, Granzier H, Gussoni E, Lawlor MW: Tissue triage and freezing for models of skeletal muscle disease. J Vis Exp 2014:51586
26. Liu H, Sadygov RG, Yates JR 3rd: A model for random sampling and estimation of relative protein abundance in shotgun proteomics. Anal Chem 2004, 76:4193−4201
27. Perez-Riverol Y, Bai J, Bandla C, García-Seisdedos D, Hewapathirana S, Kamatchinathan S, Kundu Deepti J, Prakash A, Frericks-Zipper A, Eisenacher M, Walzer M, Wang S, Brazma A, Vizcaíno Juan A: The PRIDE database resources in 2022: a hub for mass spectrometry-based proteomics evidences. Nucleic Acids Res 2021, 50:D543−D552
28. Krämer A, Green J, Pollard J Jr, Tugendreich S: Causal analysis approaches in ingenuity pathway analysis. Bioinformatics 2014, 30: 523−530
29. Lawlor MW, Viola MG, Meng H, Edelstein RV, Liu F, Yan K, Luna EJ, Lerch-Gaggl A, Hoffmann RG, Pierson CR, Buj-Bello A, Lachey JL, Pearsall S, Yang L, Hillard CJ, Beggs AH: Differential muscle hypertrophy is associated with satellite cell numbers and Akt pathway activation following activin type IIB receptor inhibition in Mtm1 p.R69C mice. Am J Pathol 2014, 184: 1831−1842
30. Schneider CA, Rasband WS, Eliceiri KW: NIH Image to ImageJ: 25 years of image analysis. Nat Methods 2012, 9:671−675
31. Garcia-Cazarin ML, Snider NN, Andrade FH: Mitochondrial isolation from skeletal muscle. J Vis Exp 2011:2452
32. Sivandzade F, Bhalerao A, Cucullo L: Analysis of the mitochondrial membrane potential using the cationic JC-1 dye as a sensitive fluorescent probe. Bio Protoc 2019, 9:e3128
33. Méchin V, Damerval C, Zivy M: Total protein extraction with TCA-acetone. Methods Mol Biol 2007, 355:1−8
34. Delahunty C, Yates JR 3rd: Protein identification using 2D-LC-MS/MS. Methods 2005, 35:248−255
35. Huang R, Grishagin I, Wang Y, Zhao T, Greene J, Obenauer JC, Ngan D, Nguyen D-T, Guha R, Jadhav A, Southall N, Simeonov A, Austin CP: The NCATS BioPlanet—an integrated platform for exploring the universe of cellular signaling pathways for toxicology, systems biology, and chemical genomics. Front Pharmacol 2019, 10: 445
36. Rachakonda G, Xiong Y, Sekhar KR, Stamer SL, Liebler DC, Freeman ML: Covalent modification at Cys151 dissociates the electrophile sensor Keap1 from the ubiquitin ligase CUL3. Chem Res Toxicol 2008, 21:705−710
37. Mills EL, Ryan DG, Prag HA, Dikovskaya D, Menon D, Zaslona Z, Jedrychowski MP, Costa ASH, Higgins M, Hams E, Szpyt J, Runtsch MC, King MS, McGouran JF, Fischer R, Kessler BM, McGettrick AF, Hughes MM, Carroll RG, Booty LM, Knatko EV, Meakin PJ, Ashford MLJ, Modis LK, Brunori G, Sévin DC,

Fallon PG, Caldwell ST, Kunji ERS, Chouchani ET, Frezza C, Dinkova-Kostova AT, Hartley RC, Murphy MP, O'Neill LA: Itaconate is an anti-inflammatory metabolite that activates Nrf2 via alkylation of KEAP1. Nature 2018, 556:113−117

38. Brand MD, Nicholls DG: Assessing mitochondrial dysfunction in cells. Biochem J 2011, 435:297−312
39. Feng JJ, Marston S: Genotype-phenotype correlations in ACTA1 mutations that cause congenital myopathies. Neuromuscul Disord 2009, 19:6−16
40. de Winter JM, Ottenheijm CAC: Sarcomere dysfunction in nemaline myopathy. J Neuromuscul Dis 2017, 4:99−113
41. Pappas CT, Bhattacharya N, Cooper JA, Gregorio CC: Nebulin interacts with CapZ and regulates thin filament architecture within the Z-disc. Mol Biol Cell 2008, 19:1837−1847
42. Bang ML, Mudry RE, McElhinny AS, Trombitás K, Geach AJ, Yamasaki R, Sorimachi H, Granzier H, Gregorio CC, Labeit S: Myopalladin, a novel 145-kilodalton sarcomeric protein with multiple roles in Z-disc and I-band protein assemblies. J Cell Biol 2001, 153: 413−427
43. Ma K, Wang K: Interaction of nebulin SH3 domain with titin PEVK and myopalladin: implications for the signaling and assembly role of titin and nebulin. FEBS Lett 2002, 532:273−278
44. McElhinny AS, Kolmerer B, Fowler VM, Labeit S, Gregorio CC: The N-terminal end of nebulin interacts with tropomodulin at the pointed ends of the thin filaments. J Biol Chem 2001, 276:583−592
45. Ohlendieck K: Proteomic identification of biomarkers of skeletal muscle disorders. Biomarkers Med 2013, 7:169−186
46. Ohlendieck K: Proteomics of skeletal muscle differentiation, neuromuscular disorders and fiber aging. Expert Rev Proteomics 2010, 7: 283−296
47. Balchin D, Hayer-Hartl M, Hartl FU: In vivo aspects of protein folding and quality control. Science 2016, 353:aac4354
48. Chiti F, Dobson CM: Protein misfolding, amyloid formation, and human disease: a summary of progress over the last decade. Annu Rev Biochem 2017, 86:27−68
49. Mogk A, Bukau B, Kampinga HH: Cellular handling of protein aggregates by disaggregation machines. Mol Cell 2018, 69: 214−226
50. Pakos-Zebrucka K, Koryga I, Mnich K, Ljujic M, Samali A, Gorman AM: The integrated stress response. EMBO Rep 2016, 17: 1374−1395
51. Bellezza I, Giambanco I, Minelli A, Donato R: Nrf2-Keap1 signaling in oxidative and reductive stress. Biochim Biophys Acta Mol Cell Res 2018, 1865:721−733
52. Tonelli C, Chio IIC, Tuveson DA: Transcriptional regulation by Nrf2. Antioxid Redox Signal 2018, 29:1727−1745
53. Crilly MJ, Tryon LD, Erlich AT, Hood DA: The role of Nrf2 in skeletal muscle contractile and mitochondrial function. J Appl Physiol (1985) 2016, 121:730−740
54. Kasai S, Shimizu S, Tatara Y, Mimura J, Itoh K: Regulation of Nrf2 by mitochondrial reactive oxygen species in physiology and pathology. Biomolecules 2020, 10:320
55. Sun Q, Chen G, Streb JW, Long X, Yang Y, Stoeckert CJ Jr, Miano JM: Defining the mammalian CArGome. Genome Res 2006, 16:197−207
56. Miano JM: Role of serum response factor in the pathogenesis of disease. Lab Invest 2010, 90:1274−1284
57. Kuwahara K, Barrientos T, Pipes GC, Li S, Olson EN: Muscle-specific signaling mechanism that links actin dynamics to serum response factor. Mol Cell Biol 2005, 25:3173−3181
58. Vitadello M, Doria A, Tarricone E, Ghirardello A, Gorza L: Myofiber stress-response in myositis: parallel investigations on patients and experimental animal models of muscle regeneration and systemic inflammation. Arthritis Res Ther 2010, 12:R52
59. Alger HM, Rayavarapu S, Nagaraju K: Measurement of activation of the endoplasmic reticulum stress response in autoimmune myositis. Methods Enzymol 2011, 489:207−225
60. Durham WJ, Aracena-Parks P, Long C, Rossi AE, Goonasekera SA, Boncompagni S, Galvan DL, Gilman CP, Baker MR, Shirokova N, Protasi F, Dirksen R, Hamilton SL: RyR1 S-nitrosylation underlies environmental heat stroke and sudden death in Y522S RyR1 knockin mice. Cell 2008, 133:53−65
61. Lee CS, Hanna AD, Wang H, Dagnino-Acosta A, Joshi AD, Knoblauch M, Xia Y, Georgiou DK, Xu J, Long C, Amano H, Reynolds C, Dong K, Martin JC, Lagor WR, Rodney GG, Sahin E, Sewry C, Hamilton SL: A chemical chaperone improves muscle function in mice with a RyR1 mutation. Nat Commun 2017, 8:14659
62. Iwasa K, Nambu Y, Motozaki Y, Furukawa Y, Yoshikawa H, Yamada M: Increased skeletal muscle expression of the endoplasmic reticulum chaperone GRP78 in patients with myasthenia gravis. J Neuroimmunol 2014, 273:72−76
63. Suzuki S, Utsugisawa K, Iwasa K, Satoh T, Nagane Y, Yoshikawa H, Kuwana M, Suzuki N: Autoimmunity to endoplasmic reticulum chaperone GRP94 in myasthenia gravis. J Neuroimmunol 2011, 237: 87−92
64. Kornfeld M: Mixed nemaline-mitochondrial "myopathy.". Acta Neuropathol 1980, 51:185−189
65. Pula S, Urankar K, Norman A, Pierre G, Langton-Hewer S, Selby V, Mason F, Vijayakumar K, McFarland R, Taylor RW, Majumdar A: A novel de novo ACTA1 variant in a patient with nemaline myopathy and mitochondrial complex I deficiency. Neuromuscul Disord 2020, 30:159−164
66. D'Agostino AN, Ziter FA, Rallison ML, Bray PF: Familial myopathy with abnormal muscle mitochondria. Arch Neurol 1968, 18: 388−401
67. Oya Y, Segawa M, Ogawa M, Goto Y, Nonaka I, Kawai M: [Congenital nemaline myopathy with mitochondrial abnormalities: an adult case report]. Rinsho Shinkeigaku 2000, 40:452−458
68. Pourmand R, Azzarelli B: Adult-onset of nemaline myopathy, associated with cores and abnormal mitochondria. Muscle Nerve 1994, 17:1218−1220
69. Jin W, Goldfine AB, Boes T, Henry RR, Ciaraldi TP, Kim E-Y, Emecan M, Fitzpatrick C, Sen A, Shah A, Mun E, Vokes V, Schroeder J, Tatro E, Jimenez-Chillaron J, Patti M-E: Increased SRF transcriptional activity in human and mouse skeletal muscle is a signature of insulin resistance. J Clin Invest 2011, 121: 918−929
70. Visegrády B, Machesky LM: Myopathy-causing actin mutations promote defects in serum-response factor signalling. Biochem J 2010, 427:41−48
71. Tinklenberg JA, Slick RA, Sutton J, Zhang L, Meng H, Beatka MJ, Vanden Avond M, Prom MJ, Ott E, Montanaro F, Heisner J, Toro R, Hardeman EC, Geurts AM, Stowe DF, Hill RB, Lawlor MW: Different mouse models of nemaline myopathy harboring Acta1 mutations display differing abnormalities related to mitochondrial biology. Am J Pathol 2023, 193:1548−1567
72. Fukunaga H, Osame M, Igata A: A case of nemaline myopathy with ophthalmoplegia and mitochondrial abnormalities. J Neurol Sci 1980, 46:169−177
73. Lamont PJ, Thorburn DR, Fabian V, Vajsar J, Hawkins C, Saada Reisch A, Durling H, Laing NG, Nevo Y: Nemaline rods and complex I deficiency in three infants with hypotonia, motor delay and failure to thrive. Neuropediatrics 2004, 35:302−306
74. Sanoudou D, Corbett MA, Han M, Ghoddusi M, Nguyen MA, Vlahovich N, Hardeman EC, Beggs AH: Skeletal muscle repair in a mouse model of nemaline myopathy. Hum Mol Genet 2006, 15: 2603−2612
75. Nguyen MA, Joya JE, Kee AJ, Domazetovska A, Yang N, Hook JW, Lemckert FA, Kettle E, Valova VA, Robinson PJ, North KN, Gunning PW, Mitchell CA, Hardeman EC: Hypertrophy and dietary tyrosine ameliorate the phenotypes of a mouse model of severe nemaline myopathy. Brain 2011, 134:3516−3529
76. Ravenscroft G, Jackaman C, Sewry CA, McNamara E, Squire SE, Potter AC, Papadimitriou J, Griffiths LM, Bakker AJ, Davies KE,

Laing NG, Nowak KJ: Actin nemaline myopathy mouse reproduces disease, suggests other actin disease phenotypes and provides cautionary note on muscle transgene expression. PLoS One 2011, 6: e28699

77. Gineste C, Le Fur Y, Vilmen C, Le Troter A, Pecchi E, Cozzone PJ, Hardeman EC, Bendahan D, Gondin J: Combined MRI and (3)(1)P-MRS investigations of the ACTA1(H40Y) mouse model of nemaline myopathy show impaired muscle function and altered energy metabolism. PLoS One 2013, 8:e61517
78. Gineste C, Duhamel G, Le Fur Y, Vilmen C, Cozzone PJ, Nowak KJ, Bendahan D, Gondin J: Multimodal MRI and (31)P-MRS investigations of the ACTA1(Asp286Gly) mouse model of nemaline myopathy provide evidence of impaired in vivo muscle function, altered muscle structure and disturbed energy metabolism. PLoS One 2013, 8:e72294
79. Polyzos AA, Lee DY, Datta R, Hauser M, Budworth H, Holt A, Mihalik S, Goldschmidt P, Frankel K, Trego K, Bennett MJ, Vockley J, Xu K, Gratton E, McMurray CT: Metabolic reprogramming in astrocytes distinguishes region-specific neuronal susceptibility in Huntington mice. Cell Metab 2019, 29:1258−1273.e11
80. Caldwell CC, Petzinger GM, Jakowec MW, Cadenas E: Treadmill exercise rescues mitochondrial function and motor behavior in the CAG140 knock-in mouse model of Huntington’s disease. Chem Biol Interact 2020, 315:108907
81. Gong YY, Liu YY, Li J, Su L, Yu S, Zhu XN, Cao XP, Xiao HP: Hypermethylation of Cox5a promoter is associated with mitochondrial dysfunction in skeletal muscle of high fat diet-induced insulin resistant rats. PLoS One 2014, 9:e113784
82. Xu Z, Lv XA, Dai Q, Ge YQ, Xu J: Acute upregulation of neuronal mitochondrial type-1 cannabinoid receptor and it’s role in metabolic defects and neuronal apoptosis after TBI. Mol Brain 2016, 9:75
83. Taylor RW, Schaefer AM, Barron MJ, McFarland R, Turnbull DM: The diagnosis of mitochondrial muscle disease. Neuromuscul Disord 2004, 14:237−245
84. Huttemann M, Lee I, Pecinova A, Pecina P, Przyklenk K, Doan JW: Regulation of oxidative phosphorylation, the mitochondrial membrane potential, and their role in human disease. J Bioenerg Biomembr 2008, 40:445−456
85. Kadenbach B, Ramzan R, Moosdorf R, Vogt S: The role of mitochondrial membrane potential in ischemic heart failure. Mitochondrion 2011, 11:700−706
86. Lardy HA, Wellman H: Oxidative phosphorylations; role of inorganic phosphate and acceptor systems in control of metabolic rates. J Biol Chem 1952, 195:215−224
87. Ranu N, Laitila J, Dugdale HF, Mariano J, Kolb JS, Wallgren-Pettersson C, Witting N, Vissing J, Vilchez JJ, Fiorillo C, Zanoteli E, Auranen M, Jokela M, Tasca G, Claeys KG, Voermans NC, Palmio J, Huovinen S, Moggio M, Beck TN, Kontrogianni-Konstantopoulos A, Granzier H, Ochala J: NEB mutations disrupt the super-relaxed state of myosin and remodel the muscle metabolic proteome in nemaline myopathy. Acta Neuropathol Commun 2022, 10:185
88. Ottenheijm CA, Buck D, de Winter JM, Ferrara C, Piroddi N, Tesi C, Jasper JR, Malik FI, Meng H, Stienen GJ, Beggs AH, Labeit S, Poggesi C, Lawlor MW, Granzier H: Deleting exon 55 from the nebulin gene induces severe muscle weakness in a mouse model for nemaline myopathy. Brain 2013, 136: 1718−1731
89. Bang ML, Li X, Littlefield R, Bremner S, Thor A, Knowlton KU, Lieber RL, Chen J: Nebulin-deficient mice exhibit shorter thin filament lengths and reduced contractile function in skeletal muscle. J Cell Biol 2006, 173:905−916